universität
wien

MASTERARBEIT / MASTER'S THESIS

Titel der Masterarbeit / Title of the Master's Thesis

„Stabilization of a high-finesse, space-proof optical cavity"

verfasst von / submitted by

Mariana Schmid, BSc

angestrebter akademischer Grad / in partial fulfilment of the requirements for the degree of

Master of Science (MSc)

Wien, 2023 / Vienna, 2023

Studienkennzahl lt. Studienblatt / degree programme code as it appears on the student record sheet:	UA 066 876
Studienrichtung lt. Studienblatt / degree programme as it appears on the student record sheet:	Masterstudium Physics
Betreut von / Supervisor:	Mag. Dr. Rainer Kaltenbaek, Privatdoz.

Acknowledgements

I would like to thank my supervisor Rainer Kaltenbaek, who always took his time to support me with the problems I had during my work as his Master student (especially programming). I would further like to thank Maxime Debiossac, who supported me not only as second supervisor but also as a friend. I also want to thank the colleagues from the Aspelmeyer group, who helped me in the lab with their experienced knowledge as well as by lending me various components I needed for our setup. Last but not least I would like to thank my family, my friends and my boyfriend Tim, who always knows how to cheer me up in stressful times.

Abstract

The primary goal of the MAQRO (Macroscopic Quantum Resonators) mission proposal is to test quantum physics at a macroscopic scale. To be precise, it aims to examine whether there are fundamental limits of quantum superpositions of massive objects in terms of size, complexity, and mass. To this end, the massive test particles have to be isolated almost perfectly from their environment. Otherwise, the known decoherence effects would limit the achievable signal-to-noise-ratio (SNR) in the measurements to be performed. This requires long free-fall times, extreme vacuum, nano-gravity, and cryogenic temperatures. These conditions can be achieved by making use of a deep space environment. The experiments conducted by MAQRO will be based on matter-wave interferometry and optomechanics with optically trapped dielectric particles. For this purpose, a stably bonded high-finesse optical cavity that can be aligned at room temperature and operated at cryogenic temperatures is needed. In this thesis, we characterize the prototype high-finesse cavity for the MAQRO mission and try to stabilize it by locking the frequency of the driving laser mode to the cavity resonance. We aim to implement this stabilization by using the Pound-Drever-Hall (PDH) locking technique. The main challenge is to find out how to satisfy the conditions and prerequisites for getting a PDH lock to work in our particular setup, by optimizing the visibility and the SNR of the signal resulting from the light detected after being reflected at the cavity input mirror. We will present how to face the challenge of optimizing and show that we are able to improve both visibility and SNR. Finally, we will give an outlook on the possible future directions of the project.

Kurzfassung

Das Hauptziel des Missionsproposals MAQRO (Macroscopic Quantum Resonators) besteht darin, die Quantenphysik auf makroskopischer Ebene zu testen. Um genau zu sein, soll untersucht werden, ob es fundamentale Grenzen von Superpositionen massiver Teilchen hinsichtlich Größe, Komplexität und Masse gibt. Um Dekohärenz zu vermeiden, müssen die Teilchen nahezu perfekt von der Umwelt abgeschirmt werden, andernfalls würden die bekannten Dekohärenzeffekte das Signal-Rausch-Verhältnis (SRV) bei den durchzuführenden Messungen begrenzen. Dies erfordert lange Zeiten im freien Fall, extremes Vakuum, Nanogravitation und kryogene Temperaturen. Eine Kombination dieser vier Voraussetzungen kann nur im Weltraum erfüllt werden. Die von MAQRO durchgeführten Experimente basieren auf Materiewelleninterferometrie und Optomechanik mit optisch gefangenen dielektrischen Teilchen. Zu diesem Zweck wird eine stabil geklebte Cavity (optischer Resonator) mit hoher Finesse benötigt, welche sowohl bei Raumtemperatur, als auch bei kryogenen Temperaturen stabil bleiben muss. Innerhalb dieser Arbeit werden wir den Prototypen der Cavity für MAQRO charakterisieren und versuchen diesen zu stabilisieren. Für die Stabilisierung der Cavity wird das sogenannte Pound-Drever-Hall (PDH) Verfahren angewandt. Das PDH Verfahren beinhaltet die Stabilisierung einer Laserfrequenz mit Hilfe einer Referenzfrequenz, welche die Resonanzfrequenz der Cavity darstellt. Hierbei ist die größte Herausforderung die notwendigen Bedingungen herauszufinden, um das PDH Verfahren für unseren speziellen Fall durchführen zu können. Dazu wird unter anderem ein höherer Interferenzkontrast und ein höheres SRV des Signals, das durch Detektieren des von der Cavity reflektieren Lichtstrahls entsteht, benötigt. Wir werden zeigen, wie wir dieser Herausforderung des Optimierens entgegentreten und dass wir tatsächlich in der Lage sind sowohl Interferenzkontrast als auch SRV zu verbessern. Abschließend geben wir einen Ausblick auf mögliche Zukunfsentwicklungen des Projekts.

Contents

Acknowledgements i

Abstract iii

Kurzfassung v

1. Introduction 1

2. Theoretical background 3
2.1. The MAQRO mission . . . 3
2.1.1. Non-interferometric experiments . . . 4
2.1.2. Matter-wave interferometric experiments . . . 4
2.2. Optical trapping . . . 6
2.3. Optical resonators . . . 7
2.3.1. Fabry-Pérot Resonator . . . 9
2.4. Gaussian beam propagation . . . 10
2.4.1. Beam waist and Rayleigh length . . . 10
2.4.2. TEM modes . . . 11
2.5. Pound-Drever-Hall locking . . . 12
2.6. The PID controller . . . 14
2.6.1. Proportional . . . 15
2.6.2. Integral . . . 15
2.6.3. Derivative . . . 15
2.7. Electro-optic modulation of a light field . . . 16

3. Cavity characterization 19
3.1. Theoretical parameters . . . 19
3.2. Experimental determination of the parameters . . . 20
3.2.1. Sideband creation . . . 21
3.2.2. FSR & coupling efficiency measurements . . . 24
3.2.3. Linewidth measurements . . . 26

4. Cavity locking 29
4.1. The reflected cavity signal . . . 29
4.2. Improvement using an amplifier . . . 32
4.3. The PID . . . 34
4.4. Building the filtering cavity . . . 35
4.5. Results with the filtering cavity . . . 41

5. Conclusion and Outlook **45**
5.1. Visibility and SNR of the reflected high-finesse cavity signal 45
5.2. The locking scheme 45
5.3. Improvement of visibility and SNR 46
5.4. Outlook 47

Bibliography **49**

A. Appendix **53**

B. List of Programs **65**
B.1. Python scripts 65
B.2. Mathematica scripts 66

1. Introduction

The MAQRO (Macroscopic Quantum Resonators) mission proposal aims to examine the fundamental limits of quantum superpositions concerning the size, complexity, and mass of mesoscopic test particles [1–3]. In particular, the proposed experiments intend to create center-of-mass superpositions of test masses with displacements and free evolution times that, in combination, go far beyond what is currently achievable on earth. To this end, the massive test particles have to be isolated almost perfectly from their environment to prevent the decoherence of the quantum states investigated. Therefore, the MAQRO proposal aims to make use of deep space to achieve long free-fall times, extreme vacuum, nano-gravity, and cryogenic temperatures [3–5]. In order to go significantly beyond the current state of the art, MAQRO proposes to use several technological advances in space technology [2, 3] and in the fields of quantum optics, matter-wave interferometry and optical trapping. Moreover, the success of MAQRO will also depend on the development of new key technologies that are of particular interest in a space setting. One of these technologies are stably bonded high-finesse optical cavities that can be aligned at room temperature and used at the cryogenic operating temperatures required for MAQRO. Additionally, these cavities and their alignment have to be sufficiently robust to withstand the accelerations occurring during a mission launch.

In this thesis, the objectives are to characterize a prototype cavity for the MAQRO mission and to lock the frequency of the optical pump to the cavity resonance by using the Pound-Drever-Hall (PDH) locking technique [6, 7]. The cavity is a high finesse cavity (several 10^4) consisting of two free-standing cavity mirrors, and with a relatively long cavity length of ~ 10 cm, as is envisioned for the MAQRO mission [3]. This results in a narrow linewidth on the order of 10 kHz, which is beneficial for side-band-resolved optomechanical cooling, but it also results in a high sensitivity to vibrations. Due to that, the main task will be to determine the requirements necessary for achieving a stable PDH lock. Here, the main problem that has to be overcome is to achieve a low-noise error signal. This is more challenging than expected, since the experiment is limited in multiple ways. One of the main limitations of the signal-to-noise-ratio (SNR) is the distribution of the optical power into many sidebands, which arise from our modified way to implement the PDH lock. In the end, we decided to build a filtering cavity in order to improve the SNR. This should lead to a reflected signal of the prototype cavity with higher visibility than without filtering cavity, which we expect to result in an improved error signal. We intend to later use this improved error signal for the PDH lock.

The thesis is structured in the following way: In chapter 2, the theoretical background that is needed to understand and conduct the experimental part will be described. Here, we will provide an overview of the MAQRO mission (section 2.1), optical trapping (section 2.2), optical resonators (section 2.3), gaussian beam propagation (section 2.4), the Pound-Drever-Hall locking technique (section 2.5), the working principle of PID control (section 2.6) and the electro-optic modulation of a light field (section 2.7). After that, we will discuss the experimental part. First, we will characterize the cavity with both the expected and the experimental values (chapter 3). Then we will describe the cavity locking (chapter 4), of how the filtering cavity was built (4.4) and how the use of a filtering cavity impacted the signal-to-noise ratio 4.5. Finally, we will discuss the results of our work, and we will provide an outlook for possible next steps and future developments (chapter 5).

2. Theoretical background

2.1. The MAQRO mission

One prediction of quantum physics is that systems of arbitrary complexity and size can be prepared in superpositions of distinct states [1]. Although it contradicts our intuitive understanding of reality, this prediction has already been confirmed for large particles on the order of 3×10^4 atomic mass units (amu) and consisting of up to 2000 atoms by using Talbot–Lau interferometry [8]. Some alternative theoretical models predict deviations from the laws of quantum physics as we know them today for large test masses or for superpositions with large spatial displacements. However, ground-based experiments (like the experiments using Talbot-Lau intererometry as mentioned above) are limited concerning the size and mass of test particles, since they would require extremely long free-fall times and have to be almost perfectly isolated from the environment, which is not possible on earth due to vibrations and gravitational field-gradients [2]. This is the reason why the MAQRO mission suggests to make use of deep space. A guiding principle in the design of MAQRO has been the endeavour to harness the cryogenic temperatures and the vacuum conditions of deep space [2, 3, 9]. If one properly shields the payload from the hot surfaces of the spacecraft and from space radiation, it may be possible to achieve the necessary requirements for preparing and observing massive superpositions over long free-fall times [4, 5, 10]. The MAQRO experiments are based on matter-wave interferometry and optomechanics with optically trapped dielectric particles. After the particles are cooled to the quantum ground state, they are released from the trap. Then their wave packet expands and the particles evolve freely for a long period of time. For the matter-wave interferometry, the particles are prepared in a superposed quantum state after some time t_1. After some additional time of free evolution t_2, their position will be detected. The main goals of the MAQRO mission are to examine

- the predictions of quantum physics in parameter regimes that were already achieved in experiments on ground, in order to test that the measurements are working, to calibrate the MAQRO instrument and to see how much decoherence the test particles experience in the space environment (black body radiation, collisions with gas particles, scattering of charged particles, thermal expansion of the optical bench, measurement inaccuracies etc.)

- standard decoherence effects with test particles going beyond the current limits concerning size and mass in ground-based experiments

- gravitational decoherence

There are also some additional goals that might be achieved as well, namely to test decoherence on rotational quantum revivals and to use the macroscopic quantum systems as detectors for dark or exotic matter [1, 11–16], but this is not the focus of this thesis. Once the payload is launched to space, matter-wave interferometric and non-interferometric tests will be performed, which will be further discussed in the following subsections.

2.1.1. Non-interferometric experiments

MAQRO offers the possibility to observe the heating of the motion of a trapped particle, due to decoherence effects [2, 17]. The goal is to determine possible deviations from the predictions of quantum mechanics. If there are any deviations, this would lead to an increasing mean occupation number of the quantum harmonic oscillator that describes the motion of the trapped particle. This experiment does not require free falling tests, but it could benefit from MAQRO's isolation from the environment.

Furthermore, the influence of the space environment on the wave-packet expansion could be observed with MAQRO. Quantum physics predicts that after releasing the particle from its trap, the wave-packet that describes the quantum state of the particle would expand. If there are any deviations from quantum physics the wave-packet would expand at a different rate, for example due to stochastic momentum transfer leading to a random walk [18]. In order to observe this, the width of the particle's wave-packet after some time of free evolution would be measured [17].

Those experiments would allow to determine the so called decoherence parameter Λ that incorporates deviations from quantum physics due to long-wavelength interactions [18, 19]. Also, it allows to determine new sources of decoherence if we observe deviations from quantum physics and if the experiment is isolated from all known sources.

2.1.2. Matter-wave interferometric experiments

The most sensitive experiment in the MAQRO payload is a high-mass matter-wave interferometer. In the current baseline design of MAQRO [2], the working principle is based on the near-field interferometry as described in the work of Bateman et al [20]. This design is based on a combination of preparing the initial quantum state using optomechanical cooling plus the preparation of a superposition state using a single optical grating to observe Talbot-Lau matter-wave interferometry. In the most recent version of the proposal [1], the design of the MAQRO payload has been adapted to allow for optomechanical ground-state cooling via coherent scattering into a high-finesse optical cavity [1]. The sensitivity of such matter-wave interferometers to deviations from quantum physics is determined by how well the test particle is isolated from known decoherence effects, as well as by measurement statistics and by measurement precision.

Talbot-Lau interferometry is usually performed by using three gratings. The first one acts as the coherent source of massive particles. The second prepares the particles in a superposition state and the third one is an absorptive grating, which allows to determine the presence of a periodic interference pattern, which occurs due to the Talbot effect. Since material gratings have the disadvantage to interact with the test particle via the van-der-Waals interaction, the newer approaches replace the central grating by an optical standing wave grating. In this case, the light in the grating induces a dipole moment in the test particle, which in turn interacts with the optical grating. This phase shift will depend on the position where a test particle passes through the grating. However, the particles can absorb or scatter some of the light, which would heat up the particles and lead to enhanced decoherence via the scattering and absorption of blackbody radiation. The excessive energy may even lead to a fragmentation or damage of the test particle. The research group of Markus Arndt developed an interferometer that even uses three optical gratings (OTIMA) [8, 21, 22]. Here, the wavelength of the laser is chosen such that the light is ionizing the test particles passing through an anti-node of the grating after absorption of a photon. Those ionized particles will be discarded using a homogeneous electric field. Those particles that are not ionized are forwarded to detection. For MAQRO, however, the interferometric approach will be a bit modified, as already described above. Here, there is no grating used as coherent source, but a high-finesse cavity to allow sideband cooling [23]. The particle is trapped and its motion is cooled in all spatial directions, such that the initial quantum state is as pure as possible. This mechanism will be further explained in section 2.2. Then the particle is released and its wave function will expand for a certain amount of time t_1. After that time, another beam of light (orthogonal to the trapping one) is switched on to implement a phase grating. The phase of this beam will be imprinted on the quantum state of the center-of-mass motion of the particle [2, 20]. After that, the state evolves freely for another amount of time t_2. Finally, the position of the particle is measured. This whole procedure is repeated a sufficient amount of times until the measurement data become statistically relevant enough for reconstructing the interference pattern. The free evolution time of the particle should in total be $t_1 + t_2 \approx 100$ s. The total amount of time should ideally be as long as possible, but there are some limitations: if the evolution time is too large, the increase of the wave packet would become too large for using optical scattering to detect the position of the particle. Furthermore, the evolution time is limited by the mission life time. This limits the duration of each measurement series and therefore the time of free evolution available for each data point [17, 24].

In order to perform the experiments described above, one needs a high-finesse cavity to cool the center-of-mass motion of the test particle that fulfills some special conditions. It has to be comparatively long, since we want the mirrors to be as far away as possible from our trapped particle. Otherwise the mirrors could shield the particle such that it is possibly not exposed enough to the cryogenic temperatures of deep space. Plus, the cavity needs to have a high finesse of at least 30000 (and therefore a narrow linewidth) which is needed to cool the test particle close to its quantum ground state [9]. Also, since the cavity will be aligned at room temperature, the various parts of the cavity setup may experience different thermal expansion in the cool-down process if one uses different materials. This might also occur in cases where parts of the setup cool down at different rates due to a lack of thermal conductivity in the interfaces between the elements. To counteract these effects, the baseplate of the cavity was chosen to be made of silicon carbide and the remaining optical elements are made of fused silica, which are known to have very low coefficients of thermal expansion. This leads to a cavity that is even stable while experiencing thermal fluctuations [1, 2, 10].

2.2. Optical trapping

The experiments proposed for the MAQRO mission rely on the use of optically trapped dielectric particles. In this section, we will review the basics of optical trapping techniques.

Single-beam gradient force traps are also known as optical tweezers. The reason is that one can imagine the laser beam as a tweezer that is able to optically hold and manipulate a particle very precisely. In order to achieve that, the laser beam has to be focused with a lens of high numerical aperture (NA). At the beam waist, which is the narrowest point of a focused laser beam (see more in section 2.4), the electric field gradient is the strongest [25, 26]. In the presence of a laser beam, a dielectric particle will be attracted to that point. The attraction to stronger fields occurs because dielectric particles are usually optically denser than the medium surrounding the particle [27].

Due to the momentum transfer of the scattered incident photons, the particle experiences a force [25]. This force can be split into two components - the scattering force and the gradient force. The gradient force acts in the direction of the spatial light gradient, since the particle is attracted to the point of the strongest field. The scattering force is the more intuitive one, since it is a direct consequence of momentum transfer from the photons of the trapping beam to the dielectric particle [28]. However, the light is scattered not only in one direction but it can be scattered in any direction, depending on the geometry of the particle. If the scattering is isotropic, the resulting forces cancel each other except in the direction of light propagation. There also exists the gradient force which acts in the direction of the spatial light gradient. This must be considered if the electric field gradient is strong, such as close to or at the focus of a laser beam. In this case, the laser induces fluctuating dipoles in the dielectric particle. The interaction of these dipoles with the electric field at the focus increases the trapping force due to the gradient field. This force is proportional to the polarizability of the particle as well as to the optical intensity gradient at the focus. In order to achieve stable trapping, the gradient force that pulls the particle to one location has to dominate over the scattering force that pushes the particle away from that region. A schematic is shown in figure 2.1.
In the experiment described in this thesis, the future trapping will be performed with the Gaussian TEM_{00} mode (see more in section 2.4), since there the beam is focused very tightly and therefore achieves higher field intensities.

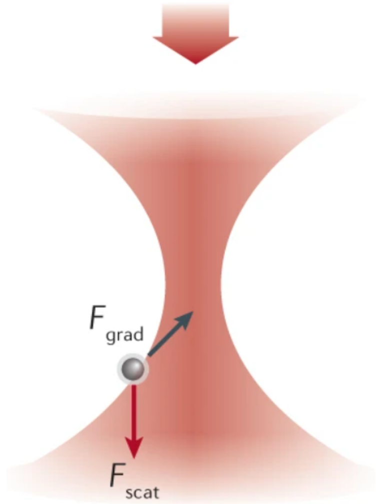

Figure 2.1.: Illustration of an optical tweezer, taken from the work of Bustamante et al [29]. The laser is focused using a high NA lens. F_{grad} stands for the gradient force that pulls the particle to the center of the beam and F_{scat} for the scattering force that pushes the particle away from the beam.

2.3. Optical resonators

Since this thesis is about characterizing a high-finesse cavity, this section gives an overview about the physics of optical resonators. We will especially describe the Fabry-Pérot resonator, which is the resonator used in the underlying experiment.

An optical resonator consists of at least two curved mirrors (exactly two mirrors in the case of a Fabry-Pérot resonator) that trap an incoming light beam by reflecting and refocusing the beam for many round trips [30]. Whether a steady-state field can be established inside the cavity depends on the wavelength λ of the incoming light beam and the cavity length L. It also depends on the wavefront curvature matching the curvature of the cavity mirrors (see section 3.1). However, here we will focus on the resonance condition. To be precise, that resonance condition is determined by the following formula [31]

$$\lambda_q = \frac{2nL}{q} \tag{2.1}$$

Here, n stands for the refractive index of the medium between the mirrors and q for the integer number of intensity maxima [31]. The resonance condition is fulfilled for any λ fulfilling equation 2.1. The difference between next-neighbour resonances $\nu = \frac{c}{\lambda}$ is [31]

$$\Delta\nu_{\mathrm{FSR}} = \frac{c}{\lambda_q} - \frac{c}{\lambda_{q+1}} = \frac{c}{2nL} \tag{2.2}$$

The constant c denotes the speed of light and $\Delta\nu_{\mathrm{FSR}}$ is called the free spectral range.

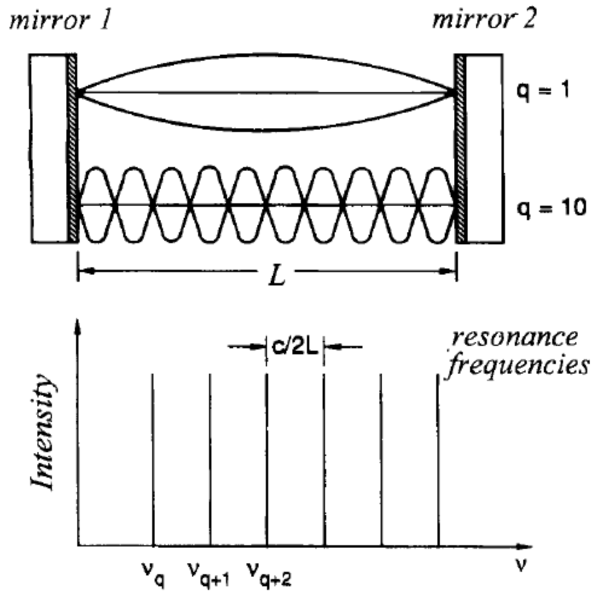

Figure 2.2.: Illustration of an optical resonator, taken from the work of Hodgson and Weber [31]. The upper panel shows the basic principle with two mirrors separated by a certain length L. It shows two cases of steady-state field creation, for $q = 1$ and $q = 10$. The lower panel shows the separation of several resonance frequencies.

Figure 2.2 demonstrates the layout of an optical resonator as well as the modes satisfying the resonance condition. It is an idealized version where the reflectivities of mirrors 1 and 2 are both assumed to be 100%. In reality, the resonance peaks will become broader for higher losses inside the resonator, due to transmission and absorption factors of the mirrors. The cavity linewidth $\Delta\nu$ is defined as the full width at half maximum (FWHM) of the transmitted or reflected cavity peaks. Another characteristic property of cavities is the finesse $\mathcal{F}$. The ideal finesse without taking into account any losses is defined as [32]

$$\mathcal{F} = \frac{\pi\sqrt{R}}{1-R} \tag{2.3}$$

It is also described as the amount of times the cavity linewidth fits into the FSR

$$\mathcal{F} = \frac{\Delta\nu_{\mathrm{FSR}}}{\Delta\nu} \tag{2.4}$$

2.3.1. Fabry-Pérot Resonator

As we already mentioned above, a Fabry-Pérot cavity consists of exactly two mirrors with reflection and transmission coefficients R_1, T_1, R_2 and T_2 [31, 32]. The numeric index indicates the number of the mirror (1 or 2). A monochromatic light beam at some wavelength λ and with an electric field E_{in} (intensity I_{in}) will be coupled into the resonator via mirror 1. The transmitted part will be reflected back and forth between mirrors 1 and 2. At each roundtrip, some of the intensity will be coupled out of the cavity at both mirrors, leading to a reflected and a transmitted light field E_{r} and E_{t} [32]

$$E_{\text{r}} = E_{\text{in}} \frac{r_1 - r_2 e^{i\delta}}{1 - r_1 r_2 e^{i\delta}} \tag{2.5}$$

$$E_{\text{t}} = E_{\text{in}} \frac{t_1 t_2}{1 - r_1 r_2 e^{i\delta}} \tag{2.6}$$

with r_1, r_2, t_1, t_2 being the reflectivity and transmissivity amplitudes and L is the cavity length. The factor $e^{i\delta}$ denotes the phase accumulated by the optical field during a full round trip. If the field is on resonance with the cavity, the phase results to be $e^{i\delta} = 1$, therefore simplifying equations 2.5 and 2.6. If one now assumes the reflectivity $R_i = |r_i|^2$ and transmission $T_i = |t_i|^2$ coefficients, the transmitted part of the intensity can be calculated according to [32]

$$I_{\text{t}} = I_{\text{in}} \frac{T_1 T_2}{|1 - \sqrt{R_1 R_2} e^{i\delta}|^2} \tag{2.7}$$

The reflected intensity is simply defined by $I_{\text{r}} = I_{\text{in}} - I_{\text{t}}$. Note that the above formulas do not take into account any losses (absorption factors). In order to reformulate the equations including losses, we first introduce the finesse coefficient F that is related to the finesse $\mathcal{F}$ in the following way [32]

$$F = \left(\frac{2\mathcal{F}}{\pi} \right)^2 \tag{2.8}$$

The generalized finesse coefficient, that introduces the loss factor A, is defined by the following formula [32]

$$F_A = \frac{4\sqrt{R_1 R_2 (1 - A)}}{[1 - \sqrt{R_1 R_2 (1 - A)})]^2} \tag{2.9}$$

The losses A include absorption and scattering into other modes. With this we can now redefine the transmitted intensity in the presence of losses as [32]

$$I_{\text{t}} = I_{\text{in}} \frac{4 T_1 T_2 (1 - A)}{(T_1 + T_2 + A)^2 \ (1 + F_A \sin^2(\delta/2))} \tag{2.10}$$

2.4. Gaussian beam propagation

This section provides an overview of the properties of Gaussian beams [32]. If the beam divergence is small, the paraxial approximation can be applied, therefore assuming Gaussian beam propagation [33]. The paraxial approximation corresponds to neglecting the second-order derivative term with respect to the spatial dimensions transverse to the direction of the beam propagation in the propagation equation. Along the direction of propagation z, a laser beam close to the source behaves like a planar wave with a constant amplitude E_0 and the corresponding field can be written as [32]

$$E(z,t) = E_0 \; exp[-i(\omega t - kz)] \tag{2.11}$$

with $k = \frac{2\pi}{\lambda}$ being the wavenumber and ω the angular frequency. However, far away from the source, the wave starts to behave like a spherical wave with a changing amplitude proportional to the inverse of the distance from the source [32]

$$E(z,t) = E_0 \; \frac{exp[-i(\omega t - kz)]}{kz} \tag{2.12}$$

The combination of both waveforms can be described by the following formula [32]

$$E(z,t) = E_0 \; \frac{exp[-i(\omega t - kz)]}{k(z - iz_0)} \tag{2.13}$$

with the region $|z| < z_0$ describing the plane wave behaviour and $|z| > z_0$ the spherical wave behaviour. Note that this approach assumes a simplification to 1D. The 3D extension is achieved by replacing kz by $\vec{k} \cdot \vec{r}$ and by expanding $\vec{k} \cdot \vec{r}$ close to the z-axis.

2.4.1. Beam waist and Rayleigh length

The radius of a laser beam w cannot stay constant over a long distance, due to diffraction. This means that it will change in the direction of propagation [33]. The radius of the beam at a position z relative to the position of the beam waist w_0 (the narrowest radius of the beam) is given by [33]

$$w(z) = w_0 \sqrt{1 + \left(\frac{z}{z_R}\right)^2} \tag{2.14}$$

Here, z_R denotes the Rayleigh length, which is defined as [33]

$$z_R = \frac{\pi w_0^2}{\lambda} \tag{2.15}$$

The Rayleigh length describes the distance from the beam waist over which the radius of the beam will increase to $\sqrt{2} w_0$ or over which the cross section doubles. An illustration of this is shown in figure 2.3. The shorter the Rayleigh length, the more focused is the beam.

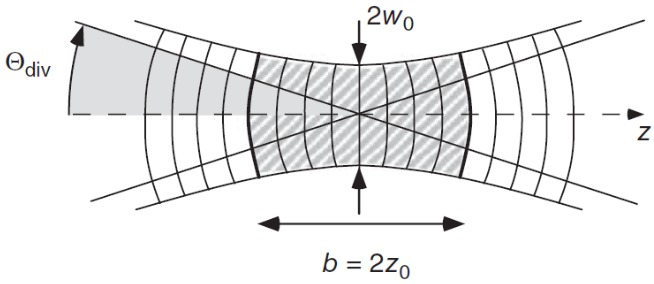

Figure 2.3.: A Gaussian beam around its narrowest radius (beam waist). The grey dashed area illustrates twice the Rayleigh length, which is known as the confocal parameter b. Θ_{div} is a parameter that describes the divergence of the beam. The picture is taken from the work of Meschede [32].

2.4.2. TEM modes

When light propagates inside an optical resonator, its intensity profile may change during propagation. However, this is not the case for some electric field amplitude distributions, called resonator modes [34]. The transverse amplitude profile reproduces itself after one full roundtrip. Those resonator modes are described by Hermite-Gaussian modes (or transverse electromagnetic TEM_{nm} modes) [35, 36]. The mathematical description of their electric field distribution $E_{nm}(x, y, z)$ consists of the product of a Gaussian function describing the shape of the profile in the z direction of propagation and a Hermite polynomial describing it in the x and y direction. This is a solution of the wave equation resulting from paraxial approximation [35]

$$\begin{aligned} E_{nm}(x,y,z) = E_0 \frac{w_0}{w(z)} \times \\ H_n\left(\sqrt{2}\frac{x}{w(z)}\right) e^{-\frac{x^2}{w(z)^2}} \times \\ H_m\left(\sqrt{2}\frac{y}{w(z)}\right) e^{-y\frac{y^2}{w(z)^2}} \times \\ e^{-i[kz-(1+n+m)\arctan\left(\frac{z}{z_R}\right)+\frac{k(x^2+y^2)}{2R(z)}]} \end{aligned} \tag{2.16}$$

The H_n Hermite polynomial describes the profile shape in x direction and the H_m in y direction. The fundamental TEM_{00} mode is therefore only described by the Gaussian part in the z direction, since $H_0 = 1$. Figure 2.4 shows what the modes for different orders look like.

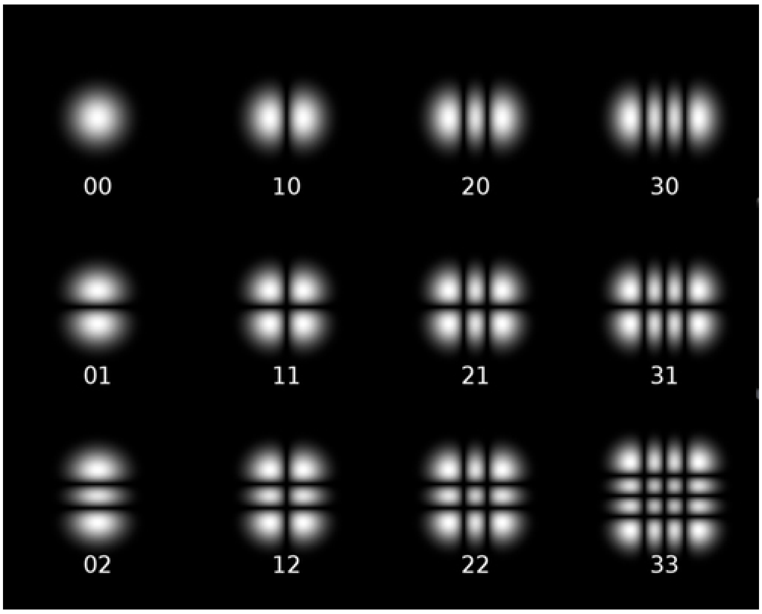

Figure 2.4.: TEM modes for different orders n,m. The picture has been taken from the work of Forget [37].

2.5. Pound-Drever-Hall locking

The following description of Pound-Drever-Hall (PDH) locking is based on the work of Black [7]. The idea behind the PDH method is to measure the difference of a laser's frequency with respect to an optical resonator, and to feed this measurement back to the laser in order to lock the frequency of the laser to the resonance frequency of the optical resonator [6, 7]. Usually, one can tune the laser via two input ports, a fast and a slow one. The fast one typically involves a piezo transducer that directly affects the resonator frequency. The slow input allows for a wider tuning of the laser frequency to compensate long-term drifts. The problem is that one does not know in which direction the laser has to be adjusted. A good method to determine that is to measure the signal reflected by the cavity [38]. The power of the light reflected by the cavity should show a dip on resonance. This dip is related to the increase of transmitted cavity power. Some of the power will be absorbed as well (see formula 2.10). What exactly such a reflected cavity signal looks like is illustrated in figure 2.5. Here, one can see that the dip is symmetric around the resonance. This means that, by only looking at the reflected signal, one cannot tell in which direction the laser's frequency has to move in order to be back on resonance again. The phase accumulated by the light reflected from the cavity will accumulate a phase that is proportional to the derivative of that signal. This phase, and therefore the derivative of the function shown in figure 2.5, is asymmetric around the resonance. It therefore contains the information about the direction in which the laser has to be tuned. However, one cannot simply measure the phase of a light field by measuring the

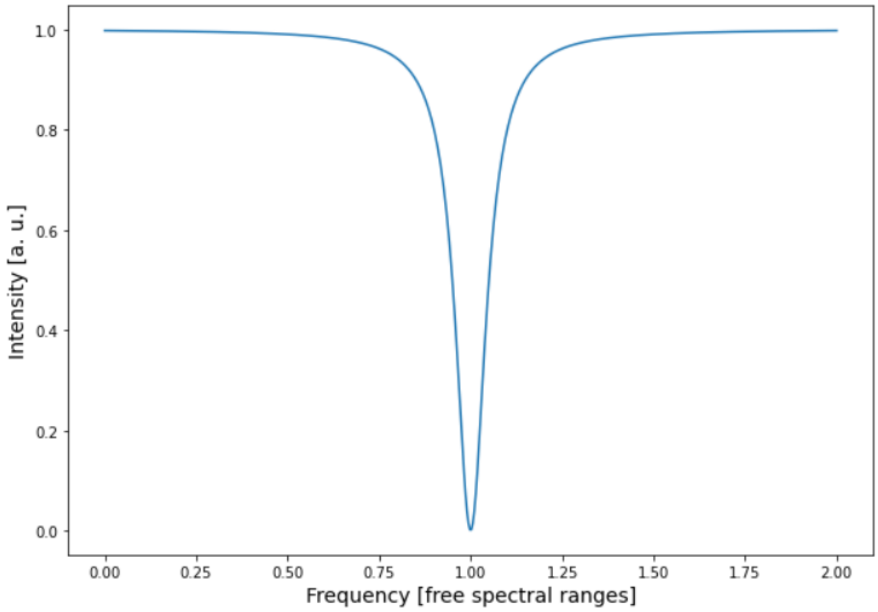

Figure 2.5.: Ideal dip in the reflected intensity. It shows that it is symmetric about resonance. However, the derivative of the function is asymmetric about resonance. The figure emulates a picture from the work of Black [7].

intensity. That is why the phase has to be measured indirectly by modulating the light beam. This can be done by using an Electro-Optic Modulator (EOM). An EOM creates sidebands at a certain modulation frequency around an input laser frequency. We will give a more detailed description of an EOM in section 2.7. The sidebands have a definite phase relationship to the incident beam, meaning that they . After measuring the reflected signal, it is mixed with a sine wave at the same frequency as the modulation frequency in order to demodulate the measured signal. This gives an error signal containing the sign in which direction the laser's frequency has to change in order to be on resonance again (see figure 2.6). With the sidebands setting a phase standard, one is therefore able to indirectly measure the phase. How the PDH lock is conducted experimentally and how the error signal is processed will be shown in chapter 4.

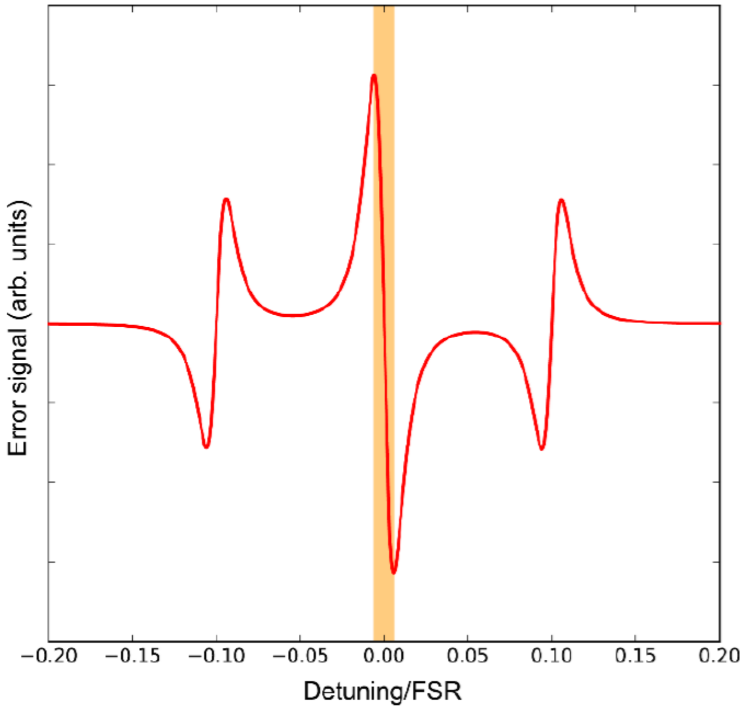

Figure 2.6.: Example error signal for a high modulation frequency (greater than the cavity linewidth). It yields the sign about the direction where the laser's frequency has to be changed. The orange shaded area approximates the region of an ideal error signal. The picture has been taken from a Moglabs manual about PDH locking [38].

2.6. The PID controller

A PID (Proportional, Integral, Derivative) controller is used to control some signal we want to stabilize with respect to a given set point [39]. Before initiating a PID lock, one first has to choose a specific set point where the signal is supposed to stay continuously. The PID constantly calculates a certain error value that tells us how far off the signal is from this set point and how to adapt the signal to get it back to the set point. Steering the signal back towards the set point can be achieved by using three different filters: Proportional, Integral and Derivative. In our case, we are using a Red Pitaya to control our error signal [40]. A Red Pitaya is an FPGA measurement tool that provides several applications, such as an oscilloscope, spectrum analyzer, PID etc. [41] There exist different models of Red Pitaya. We have been using the model "STEMlab 125-14", which has two ports for input signals and two output ports. In the following subsections, we present the functioning of each part of the PID using the Red Pitaya module "Lock-in + PID" by Marcelo Luda [40].

2.6.1. Proportional

The P part of the PID counteracts the disturbances from the set point by setting a proportional value that has the opposite sign of the disturbance. If $e(t)$ is assumed to be our input signal, then we can set a parameter [40]

$$k_p = \frac{\mathrm{PID}_{kp}}{2^{n_p}} \quad \text{with } n_p = \{0, 3, 6, 10, 12\} \tag{2.17}$$

which is controlled by the register value PID_{kp} and will be proportionally applied to $e(t)$ (see equation 2.20). The values n_p can be chosen at the user interface. The choice of possible values depends on the device's resolution. The parameters PID_{ki}, PID_{kd}, n_i and n_d, as described in the subsequent subsections for the I and D part, underlie the same logic as PID_{kp} and n_p.

If one uses only the proportional control, this would result in an equilibrium between the set point and the counteracting value, since the P controller needs an error (an offset from the set point) in order to generate the output response. However, if the P controller immediately counteracts a disturbance and sets the signal back to the set point, there exists no error. If the disturbance lasts longer, then the signal will be off the set point again. This leads to a slight permanent offset from the set point, which can be overcome with an I and D controller.

2.6.2. Integral

The I part counteracts possible disturbances by integrating the signal $e(t)$ over time. There is further a parameter $k_i = \frac{1}{\tau_i}$ applied to the integrated signal. Unlike the proportional part, it does not react immediately to a disturbance, but takes into account disturbances experienced in the past. In this way, even the offset value resulting from the P controller can be overcome. For the Red Pitaya, the parameter applied to the integrated input signal is described by [40]

$$\tau_i = \frac{2^{n_i} \times 8\ \mathrm{ns}}{\mathrm{PID}_{ki}} \quad \text{with } n_i = \{0, 3, 6, 10, 13, 16, 20, 23, 26, 30\} \tag{2.18}$$

2.6.3. Derivative

The D part of the controller depends on the parameter $k_d = \tau_d$. The D filter analyzes the trend of the error in order to make predictions how it will behave in future. According to this it will perform adjustments. The parameter applied to the derived input signal is described by [40]

$$\tau_d = \frac{2^{n_d} \times 8\ \mathrm{ns}}{\mathrm{PID}_{kd}} \quad \text{with } n_d = \{0, 3, 6, 10, 13, 16\} \tag{2.19}$$

The output signal $\mathrm{PID_{out}(t)}$ after the PID is the sum of all adjustments [40]

$$\mathrm{PID_{out}(t)} = k_p \times e(t) + \frac{1}{\tau_i} \times \int_0^t e(t')\,dt' + \tau_d \times \frac{d}{dt} e(t) \tag{2.20}$$

An illustration of how a PID signal is generated from an error signal is shown in figure 2.7.

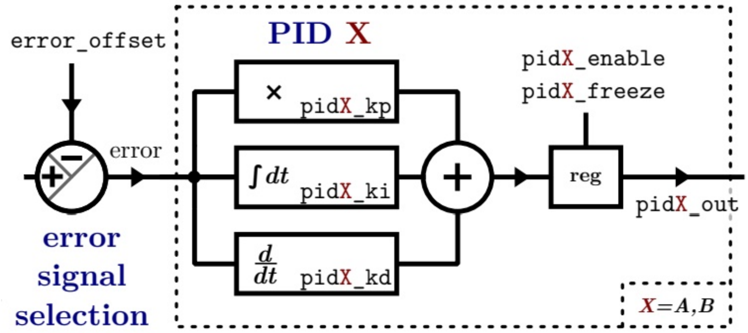

Figure 2.7.: Schematic of a PID process. The input signal is an error signal that is forwarded to a PID module that consists of proportional, integral and derivative parts. The module is able to perform two different PIDs, A and B. The adjustments of each filter are added up and give an output value $\mathrm{PID_{out}}$ that contains the information how much the input signal (error signal) has to be changed in order to reach the set point again. The picture has been taken from the work of Luda et al [40].

2.7. Electro-optic modulation of a light field

This section gives an overview of the electro-optic modulation that we apply in our setup in order to achieve PDH locking. An electro-optic modulator (EOM) uses a crystal that changes its refractive index depending on the voltage applied to it [42–44]. In this way, either the amplitude of polarized light or the frequency/phase can be modulated. Here, we will focus on the frequency modulation, since this is used in our experiment in order to create sidebands. This can be achieved by setting the polarization parallel to the principal axis of the crystal. If an oscillating electrical field with angular frequency Ω of the form [42]

$$E(t) = E_0 \sin(\Omega t) \tag{2.21}$$

is applied to the crystal, this yields the following result for the optical field after the EOM [42]

$$E_{\mathrm{EOM}}(t) = \mathrm{Re}[E_0 \exp(-i\omega t)\exp(-im \sin(\Omega t)] \tag{2.22}$$

Here, m stands for the modulation index that depends on the material parameters and the amplitude of the applied voltage. The phase ϕ of a light field with frequency ω will be modulated in the following way [42]

$$\phi(t) = \omega t + m \sin(\Omega t) \tag{2.23}$$

The resulting frequency modulation can be determined by the derivative of the phase [42]

$$\omega(t) = \omega + m\Omega \cos(\Omega t) \tag{2.24}$$

This raises the question how the sidebands we would like to use in our experiment are created with this frequency modulation. For this purpose, we expand the sine part of the resulting electric field (2.22) after the crystal by using the Bessel functions of the first kind J_i [42]

$$\begin{aligned} \exp(-im \sin(\Omega t)) = J_0(m) + 2[J_2(m) \cos(2\Omega t) + J_4(m) \cos(4\Omega t) + ...]- \\ 2i[J_1(m) \sin(\Omega t) + J_3(m) \sin(3\Omega t) + ...] \end{aligned} \tag{2.25}$$

By applying this to the whole electric field and expressing sine and cosine using exponential functions, this yields [42]

$$\begin{aligned} E_{\mathrm{EOM}}(t) = E_0\, e^{-i\omega t}\, [J_0(m) + J_1(m)\, (e^{-i\Omega t} - e^{i\Omega t})+ \\ J_2(m)\, (e^{-2i\Omega t} + e^{2i\Omega t})+ \\ J_3(m)\, e^{-3i\Omega t} - e^{3i\Omega t} + ...] \end{aligned} \tag{2.26}$$

From this expression, one can see that after the EOM there exists one peak at ω (the fundamental one from the input beam) and several other peaks at $\omega \pm n\Omega$ for n ≥ 1, called sidebands. The intensity distribution over all existing peaks is determined by the modulation depth m. For example, for a small m, almost all the power is located in the main peak ω. The larger m grows, the more power will be distributed to the higher-order peaks while the fundamental one will slowly decrease.

3. Cavity characterization

3.1. Theoretical parameters

This section is dedicated to the characterization of the high-finesse prototype cavity for MAQRO. The most important properties to characterize in a cavity were already discussed in section 2.3. The cavity consists of two mirrors with radii of curvature $r_1 = 30$ mm and $r_2 = 75$ mm and with reflection coefficients $R_1 = R_2 = (0.99997 \pm 0.00002)$. The two different radii of curvature were chosen such that the minimum waist of the fundamental cavity mode will be a distance $L/4$ from the mirror with the shorter radius of curvature, in order to achieve the highest cooling power [23]. This results in a comparatively long cavity length $L = (97.5 \pm 0.2)$ mm. The uncertainties result from the uncertainties of the radii of curvature provided by the manufacturer. According to the cavity stability diagram (see figure 3.1), the cavity length and mirror curvatures have to be in a certain ratio in order to make the cavity stable [45]. The diagram can be produced by setting the x-axis to $g_1 = 1 - \frac{L}{r_1}$ and the y-axis to $g_2 = 1 - \frac{L}{r_2}$. Here, $r_{1,2}$ denote general radii of curvature and differ from the specification provided above. The condition for a stable cavity is fulfilled if $0 < g_1 g_2 < 1$. From figure 3.1 one can see that the cavity used in this experiment lies within the stability region, as expected from the original design of the cavity.

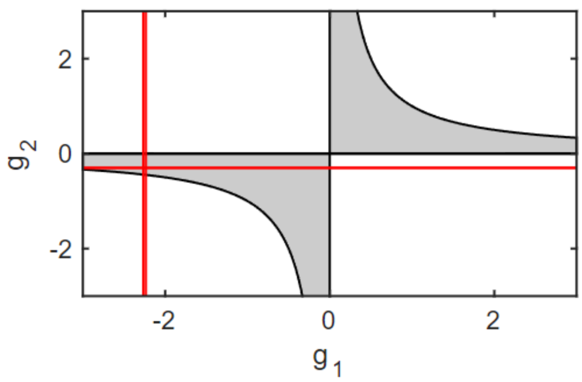

Figure 3.1.: Stability diagram of the optical cavity. The x-axis corresponds to $g_1 = 1 - \frac{L}{r_1}$ and the y-axis to $g_2 = 1 - \frac{L}{r_2}$. The grey shaded area shows in which parameter range a cavity is stable. The vertical and horizontal red lines show where the cavity used in this experiment is located. The thickness of the lines takes into account the uncertainty on the reflection coefficient and cavity length.

We use a coherent infrared laser (Mephisto) with a wavelength of $\lambda = 1064$ nm to drive and to characterize our optical cavity. Since there is only air in between the two mirrors, a refractive index of $n \approx 1$ is assumed. From formula 2.1, we can determine the number of intensity maxima inside the cavity. The result for the number of intensity maxima q within the cavity turns out to be on the order of $q \approx 10^5$, which is a large number, meaning that we can expect many intensity maxima. The free spectral range (see formula 2.2) is determined as $\Delta\nu_{\mathrm{FSR}} = (1.537 \pm 0.003)$ GHz. The uncertainty results from the cavity length L. Another important property is the finesse of the cavity. In this case, we expect an ideal finesse of $\mathcal{F} = (104718 \pm 70046)$, by using equation 2.3 and the mirror specifications provided by the manufacturer of the mirrors. From the ratio of the FSR and the finesse, we would expect a cavity linewidth of $\Delta\nu = (14.7 \pm 9.9)$ kHz (see equation 2.4).

3.2. Experimental determination of the parameters

After calculating all the theoretical characterizing values, they need to be confirmed experimentally. Figure 3.2 shows a picture of the high-finesse cavity. For this purpose, a

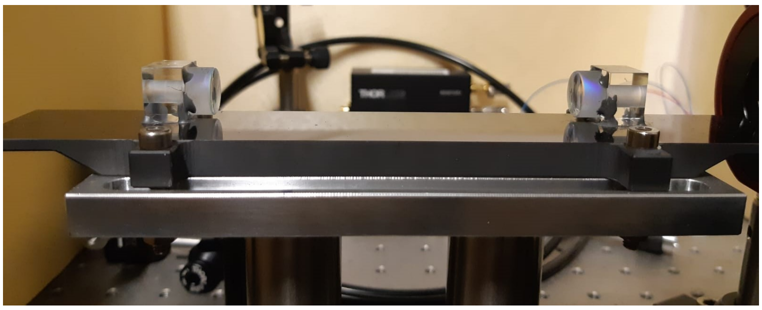

Figure 3.2.: Picture of the high-finesse cavity. The left mirror has a radius of curvature $r_1 = 30$ mm and the right one $r_2 = 75$ mm. They are glued to spacers made of fused silica, which are glued to the optical bench made of silicon carbide.

camera (PlayStation Eye) and a photodiode (New Focus, model 1623) are placed in the path of the transmitted cavity light. This allows to monitor the transmitted cavity mode as well as at the corresponding transmitted intensity. Figure 3.3 provides a schematic of the experimental setup.

The electronic circuit driving the EOM shown in figure 3.3 is partially due to the PDH lock and partially due to the way we create sidebands that differs from the standard PDH locking scheme. A more detailed description of the circuit can be found in the appendix, figure A.2.

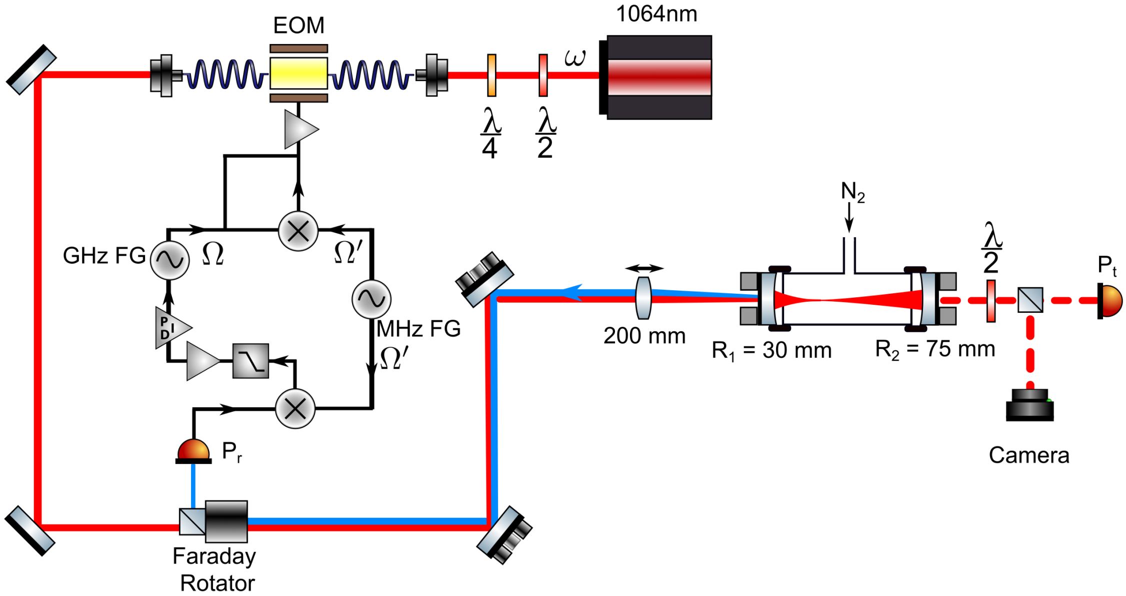

Figure 3.3.: Experimental setup for cavity characterization (including the circuit needed to implement a PDH lock). After first passing through two waveplates, the beam enters the EOM, driven by a GHz function generator (RIGOL DSG 821) mixed with a signal from a MHz function generator (Keysight 33500B Series), in order to create the sidebands required for PDH locking. Then the beam passes through a Faraday rotator (such that the back-reflected light P_r from the high-finesse cavity may be used and also to protect the laser) and finally enters the high-finesse cavity. The light P_t that is transmitted is split up by a beam splitter such that it can be detected by both a photodiode and a camera. The reflected beam is detected by another photodiode (Thorlabs, DET10C) and forwarded to the PDH locking circuit. There is an aluminum tube around the cavity with an opening that is connected to a nitrogen source.

3.2.1. Sideband creation

In section 2.5 the theoretical scheme of the PDH lock was introduced. However, due to the sharing of the laser with other experiments in the laboratory, we were not free to change the frequency of the laser without disturbing other experimental setups. Therefore, we had to implement a modified version of the PDH locking scheme. Since we cannot use the EOM created sidebands to lock the carrier frequency, we want to lock one of those sidebands instead, since we are free to change the frequency driving the EOM. We can control the frequency driving the EOM with the GHz function generator (see figure 3.3), meaning that we are able to change the sideband frequency. We need to be able to control the driving frequency of the EOM, because the sideband frequency has to be on resonance with the cavity resonance frequency. If we want to lock a sideband instead of the laser's frequency, we need something else that sets a definite phase relationship. For this purpose, we generate another couple of sidebands around the sidebands created by the GHz function generator by using a frequency mixer (Mini Circuits, ZMF-150+). The sideband frequency should be significantly larger than the linewidth, such that they are distinguishable from the center peak. We therefore choose the sideband frequency created by the MHz function generator to be $\Omega' = 10$ MHz, which is larger than the cavity linewidth $\Delta\nu = (14.7 \pm 9.9)$ kHz. One can use frequency mixers for either up- or downconversion [46]. Figure 3.4 illustrates the precise functioning. A frequency mixer

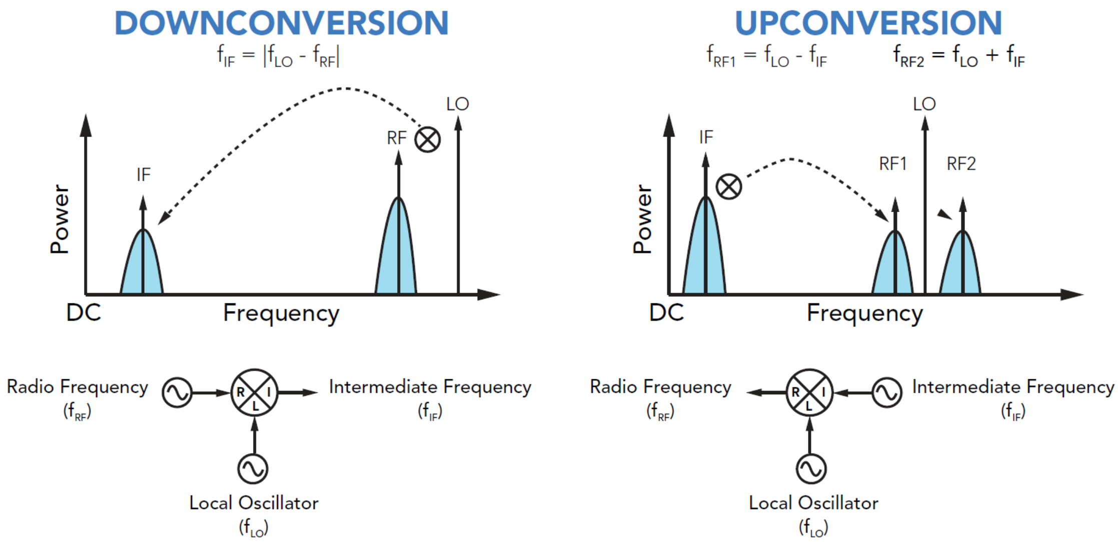

Figure 3.4.: Definitions of down- (left) and upconversion (right) of a frequency mixer. LO is the local oscillator and is given by the specifications of each mixer. IF (intermediate frequency) and RF (radio frequency) are either input or output frequency, depending on the usage (left or right). The picture has been taken from the work of Marki and Marki [46].

has three ports, two input ports and one output port: RF (radio frequency), LO (local oscillator) and IF (intermediate frequency). LO is always one input port and its frequency is given by the specifications of each mixer. If one uses a mixer in a downconverting way (figure 3.4, left), then RF is used as second input port. The IF output port will then give the difference between LO and RF: $f_{IF} = |f_{LO} - f_{RF}|$. However, if the mixer is used for upconversion (figure 3.4, right), then IF is the second input port and RF outputs the IF frequency at two positions, below and above the LO: $f_{RF} = |f_{LO} \pm f_{IF}|$.

In order to create sidebands, we use our mixer for upconversion and choose one output of the MHz FG to be the LO with a sine wave at a certain modulation frequency Ω' and the output of the RIGOL FG to be the IF at the EOM driving frequency Ω. Before sending

Ω to the mixer, it is split up in order to add it to the mixer output again later, such that we receive $\Omega \pm \Omega'$. Those frequencies are further amplified such that they have the correct power for the EOM it is finally fed to. As already described in section 2.7, the EOM creates sidebands at the driver frequency (in this case $\Omega \pm \Omega'$) around the laser frequency ω. Mathematically, the mixer output with the added frequency of the GHz function generator can be described by

$$E_{\text{out}}(t) = E_{\text{LO}} e^{i\Omega t} \frac{E_{\text{IF}}}{2} (e^{i(\Omega+\Omega')t} + e^{i(\Omega-\Omega')t}) \tag{3.1}$$

with E_{LO} being the amplitude of the LO and E_{IF} is the amplitude of the IF. $\frac{E_{\text{IF}}}{2}$ can be expressed by E_{RF}, which is the amplitude of one of the created RF output frequencies. When sending 3.1 to the EOM and by using equation 2.22 the EOM output can be described by

$$E_{\text{EOM}}(t) = E_0 e^{i\omega t + im\sin(\Omega t)} + E_0 e^{i\omega t + im\sin[(\Omega+\Omega')t]} + E_0 e^{i\omega t + im\sin[(\Omega-\Omega')t]} \tag{3.2}$$

E_0 stands for a generalized amplitude. In reality, the amplitude is different for the frequencies at ω, $\omega \pm \Omega$ and $\omega \pm \Omega \pm \Omega'$. The amplitude depends on the modulation depth m, but also on the amplitude of $E_{\text{out}}(t)$. If $m \ll 1$, we can further make the following approximation

$$E_{\text{EOM}}(t) = E_0 e^{i\omega t}[1+im\sin(\Omega t)] + E_0 e^{i\omega t}[1+im\sin[(\Omega+\Omega')t]] + E_0 e^{i\omega t}[1+im\sin[(\Omega-\Omega')t]] \tag{3.3}$$

If we express the sine by the exponential functions, this yields

$$\begin{aligned} E_{\text{EOM}}(t) = 3E_0 e^{i\omega t} &+ \frac{E_0 m}{2} e^{i(\omega+\Omega)t} - \frac{E_0 m}{2} e^{i(\omega-\Omega)t} + \\ &\frac{E_0 m}{2} e^{i(\omega+\Omega+\Omega')t} - \frac{E_0 m}{2} e^{i(\omega-\Omega+\Omega')t} + \\ &\frac{E_0 m}{2} e^{i(\omega+\Omega-\Omega')t} - \frac{E_0 m}{2} e^{i(\omega-\Omega-\Omega')t} \end{aligned} \tag{3.4}$$

The output of the EOM will therefore contain seven different frequencies, distributed as depicted in figure 3.5. The higher-order frequencies can be neglected since $m \ll 1$.

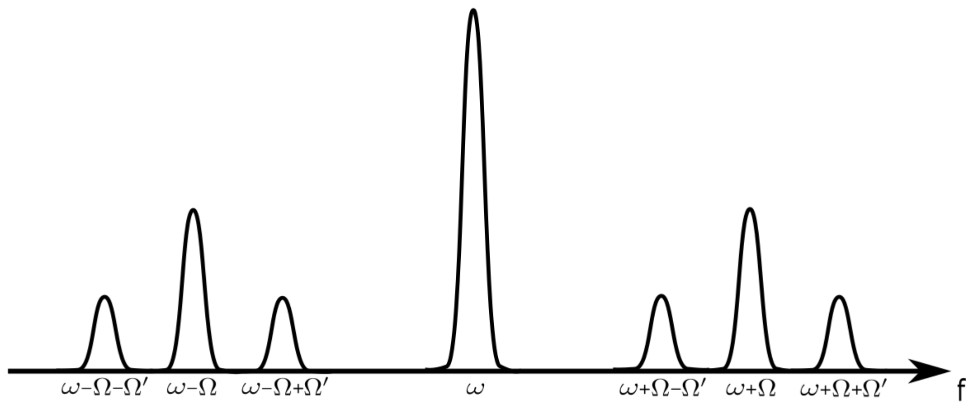

Figure 3.5.: Output frequencies of the EOM. ω is the laser frequency, Ω the frequency created by the RIGOL FG that will be locked and Ω' the frequency created by the MHz FG which is the modulation signal for the locking. Note that this is a simplified illustration and that the x- and y-axis are not true to scale.

This means that we do not directly lock the laser's frequency ω, but the sideband frequency Ω by using Ω' as modulation frequency. This allows us to bypass the need of directly modulating the laser's frequency by adjusting Ω instead. The circuit for the PDH lock will be explained in chapter 4, where we describe the locking process.

3.2.2. FSR & coupling efficiency measurements

To experimentally characterize our high-finesse cavity, we start by measuring the FSR of the cavity using the transmitted light. This can be done by monitoring the cavity transmission with the camera and measuring the interval between two frequencies applied to the EOM at which we observe the transmission of a TEM_{00} mode. For convenience, the measurement is conducted by sending the GHz function generator output directly to the EOM, bypassing the circuit that creates extra sidebands at $\pm\Omega'$. With this method, two TEM_{00} modes are measured, one at $\Omega_1 = (0.88849 \pm 0.00978)$ GHz and another one at $\Omega_2 = (0.65188 \pm 0.00978)$ GHz. Since we create two sidebands with the EOM, one at $\omega + \Omega$ and one at $\omega - \Omega$, it can happen that the TEM_{00} modes observed correspond to different sidebands. If the measurements belonged to the same sideband, then $\Delta\nu_{\mathrm{FSR}}$ would be calculated by either

$$\Delta\nu_{\mathrm{FSR}} = (\omega + \Omega_2) - (\omega + \Omega_1) = \Omega_2 - \Omega_1 \tag{3.5}$$

$$\Delta\nu_{\mathrm{FSR}} = (\omega - \Omega_2) - (\omega - \Omega_1) = \Omega_1 - \Omega_2 \tag{3.6}$$

However, when belonging to different sidebands, the calculation will be

$$\Delta\nu_{\mathrm{FSR}} = (\omega - \Omega_2) - (\omega + \Omega_1) = (\omega + \Omega_2) - (\omega - \Omega_1) = \Omega_2 + \Omega_1 \tag{3.7}$$

In our case, the two measured modes belong to different sidebands. Therefore, we add the two values $\Omega_1 + \Omega_2$, leading to an FSR of $\Delta\nu_{\mathrm{FSR}} = (1.54 \pm 0.02)$ GHz, which coincides with the theoretical expectation within the uncertainty. The error originates from the standard deviation from repeating frequency measurements of the TEM_{00} mode.
The next parameter we discuss is the coupling efficiency c_{eff}, which describes the percentage of the incoming light beam found in the TEM_{00} mode and is defined as in equation 3.8. This is the ratio of the intensity of the TEM_{00} mode divided by the sum of the intensities of all other modes within one FSR.

$$c_{\mathrm{eff}} = \frac{I_{00}}{\sum_{nm} I_{nm}} \tag{3.8}$$

I_{nm} describes the intensity of the measured TEM_{nm} mode. The modes together with their intensities and their frequencies are shown in figure 3.6.

Maximum Voltage [mV]	12.6±0.1	5.5±0.1	3.58±0.05	105±1	10.6±0.1	13.7±0.1
TEM_{nm} mode						
Frequency [GHz]	0.316	0.615	1.213	1.244	1.527	1.838

Figure 3.6.: Measurements of the intensity of each mode within one FSR. The first line is the maximum voltage measured with the photodiode. The second line shows the observed TEM_{nm} mode and the third line their position in frequency.

We perform the intensity measurements with the photodiode in the cavity transmission, by measuring the maximum peak voltage of each mode on the oscilloscope (Keysight, DSO9064A). We subtract the dark noise of the photodiode $V_{dark} = 1.46$ mV and obtain $c_{\mathrm{eff}} = (0.728 \pm 0.003) = (72.8 \pm 0.3)$ %. This means that 72.8 % of the light is coupled into the TEM_{00} mode. The coupling efficiency can be improved by walking the input beam using the two mirrors in front of the cavity (see figure 3.3). However, in practice it is hard to improve, since the cavity linewidth is narrow and the mode drifts away very fast. When following the resonance mode with the sideband created by the GHz function generator, it drifts up to a few MHz per second. To have a more stable signal for optimizing the coupling into the cavity, we periodically modulate the frequency of our sideband with a ramp signal. This allows us to effectively scan the cavity resonance within a certain frequency window, leading to a higher stability of the mode. By using this approach, we are able to improve the coupling efficiency up to $c_{\mathrm{eff}} = (79.7 \pm 0.2)$ %. The corresponding measurement data can be found in the appendix, table A.1.

3.2.3. Linewidth measurements

One of the most important properties when characterizing a cavity is the cavity linewidth. The theoretical prediction for the cavity linewidth is $\Delta\nu = (14.7\pm9.9)$ kHz (as calculated by equation 2.4) which we now want to compare with the experiment. The linewidth can be determined by measuring the transmitted or reflected cavity signal with the photodiode, while scanning the cavity at the same time using a ramp. In order to measure the intrinsic linewidth, the response time of the photodiode has to be sufficiently fast. The photodiode used in transmission has a response time of $\tau_r \leq 1$ ns for a 50 Ω termination, which is fast enough compared to the decay time of $\tau_d = \frac{1}{2\pi\Delta\nu} = (10.8\pm6.6)$ µs of the cavity [47]. One of the first cavity linewidth measurements is shown in figure 3.7.

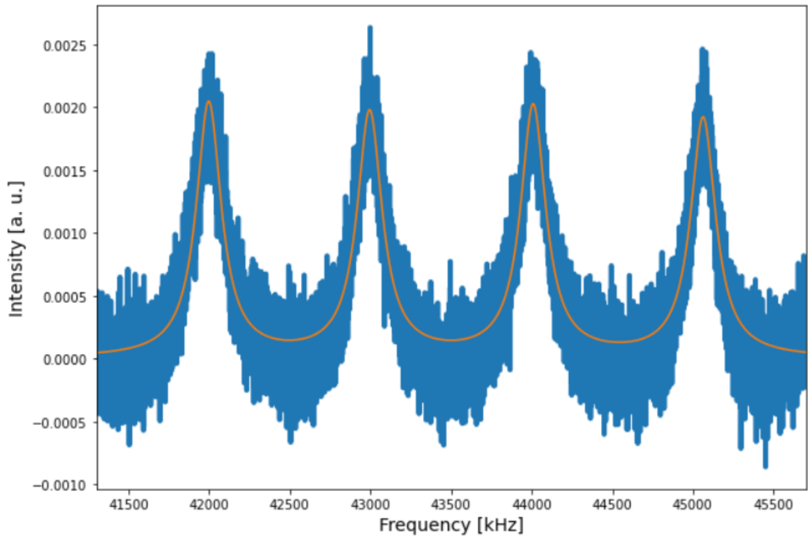

Figure 3.7.: First cavity linewidth measurement. The blue signal is the transmitted signal measured with the oscilloscope. The orange line is a Lorentzian fit.

Here, the cavity linewidth can be determined from the full width at half maximum (FWHM) of the Lorentzian fit. The fit is done for four peaks in order to determine also the uncertainty. In this case, our measurement yielded a linewidth of $\Delta\nu = (235.1\pm13.8)$ kHz, which is much broader than what we had anticipated from the specifications of the cavity mirrors. Moreover, this linewidth is incompatible with the requirements of MAQRO. In particular, this linewidth is nearly an order of magnitude broader than what we aimed for. It took us a while to realize that the laboratory in which the experiment has been conducted is very humid. We therefore suspected that the humidity has a significant influence on the mirror reflectivity. Before joining the project, some approaches to clean the mirrors already had been conducted. At the point I joined, we had established using the following protocol: The cavity mirrors are first cleaned with methanol. We further put an aluminum tube around them and seal it using viton rings in order to create vacuum.

We then pump the cavity using a primary pump that goes down to few mbar. Then the linewidth is measured again over one week. The result is shown in figure 3.8a. Right after cleaning, the linewidth is $\Delta\nu \approx 20$ kHz and then increases rapidly to reach again > 200 kHz. We realize that the sealing of the tube is not good enough to establish a vacuum. The humid air got inside quickly. The next attempt was to put nitrogen inside the aluminum tube right after cleaning the mirrors. Since nitrogen is not able to carry water, the expectation is that the mirrors will not be affected by humidity again. This time we put no vacuum, such that there is no pressure difference between the tube and the environment. The result of the linewidth measurements is shown in figure 3.8b. In the beginning, the linewidth was at around $\Delta\nu = (51.4 \pm 1.5)$ kHz, but decreased within one week to (25 ± 1) kHz. The decrease of linewidth is probably due to some remaining humidity inside the tube or on the mirror coatings that needed some time to leave the tube. The measurement was continued over one month, but the linewidth experienced no more significant changes. These results confirmed the effectiveness of our approach to protect our prototype cavity against humidity.

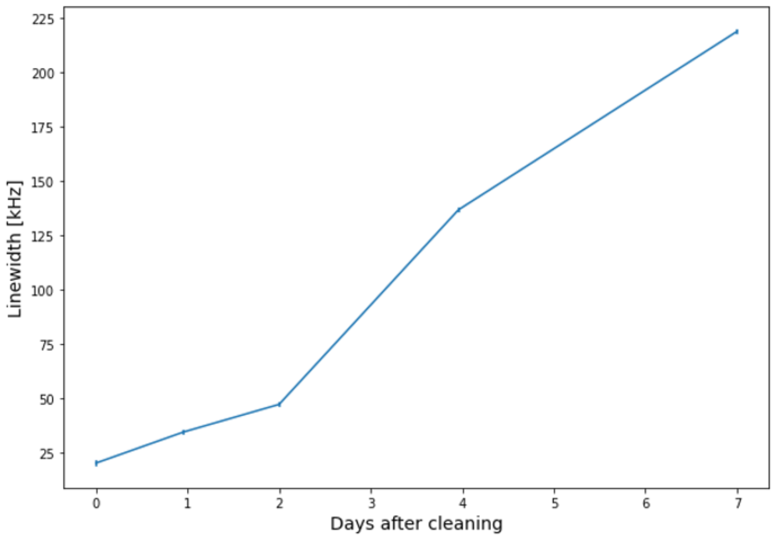

(a) Cavity linewidth versus days after cleaning the mirrors and modest vacuum. There is no nitrogen used.

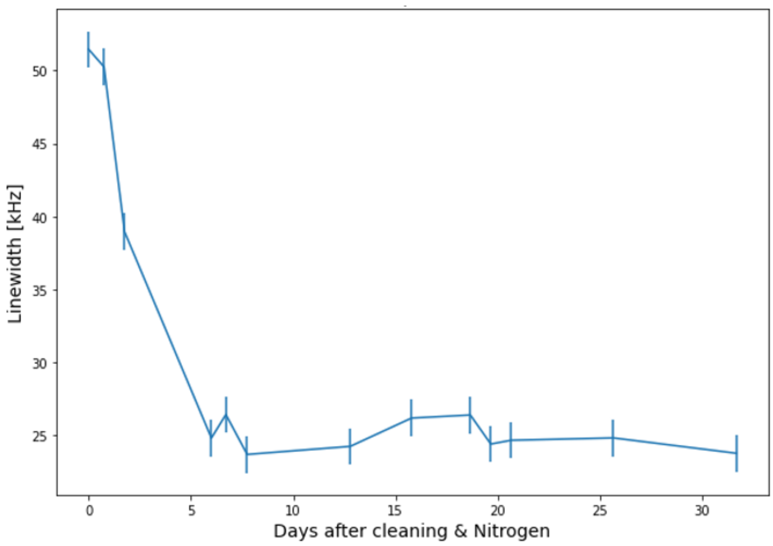

(b) Cavity linewidth versus days after cleaning the mirrors under N_2 environment.

A linewidth of $\Delta\nu = (25 \pm 1)$ kHz corresponds to a finesse of $\mathcal{F} = 61600 \pm 2400$. This is still sufficient for the future purpose of particle cooling [9].

4. Cavity locking

We now focus on the main task of this thesis, namely the locking of the laser to the optical cavity. The following chapter deals with the experimental realization of the Pound-Drever-Hall (PDH) locking technique introduced in section 2.5.

4.1. The reflected cavity signal

The PDH technique allows to lock a cavity to a reference laser or to lock the frequency of a pump mode to the resonance frequency of the optical cavity. A prerequisite for PDH locking is to detect the light of the driving laser reflected by an optical cavity. The signal resulting from detecting that light (the reflected cavity signal) will be used to create an error signal as described in section 2.5. The reflected beam first is monitored with a photodiode (Thorlabs, DET10C) while scanning over the cavity. The photodiode was chosen due to its short response time $\tau_r = 10$ ns at a 50 Ω termination, according to the manufacturer. Again, the response time has to be much shorter than the cavity decay time of $\tau_d = (10.8 \pm 6.6)$ µs. The to the maximum intensity normalized photodiode signal is shown in figure 4.1.
If the measurement data are normalized, they yield a direct measure of the visibility $\mathcal{V}$. We introduce the visibility of the of the dip seen in the reflected signal as

$$\mathcal{V} = \frac{I_{\text{max}} - I_{\text{min}}}{I_{\text{max}}} \tag{4.1}$$

with I_{max} and I_{min} being the maximum and minimum intensity, respectively. From fig. 4.1 we determine $\mathcal{V} = (5 \pm 0.5)$ %, when taking into account the background noise. The uncertainty was estimated from the oscilloscope. The signal-to-noise-ratio (SNR) is only around 3:1. Using formula 2.7 the expected transmission through the cavity is $I_\text{t} = 0.25 \times I_{\text{in}}$. This means that only 25 % of the input power will be transmitted on resonance. Since $I_\text{r} = I_{\text{in}}$ - I_t, we expect a maximum dip visibility of 25 % as well. However, this calculation was done without taking into account the power distribution into the sidebands and the losses inside the cavity. To estimate how much light is diffracted into the sidebands, we have conducted a homodyne measurement. This percentage is dependent on the modulation depth, which depends on the amplification gain of the amplifier (AmpliTech, APT3-04000800-1010-D4) before the EOM. The amplifier gain is frequency dependent (see figure A.1). Depending on the frequency generated by the GHz function generator, we expect there to be between (14±5) % and (40±5) % diffraction in one sideband (see table A.2). From this, we can conclude that, depending on the amplifier gain, we can expect the dip visibility to be between $\mathcal{V} = 3.5$ % and 10 %, without taking

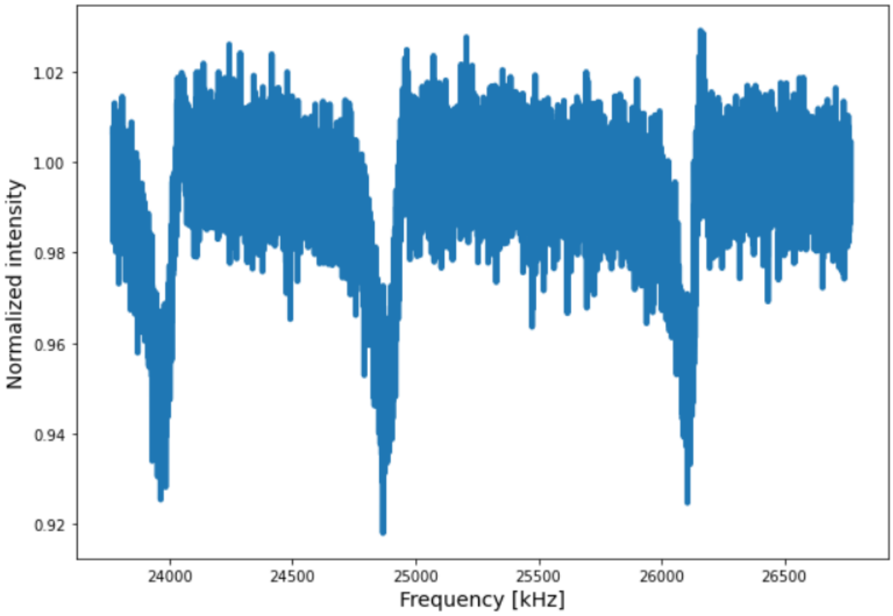

Figure 4.1.: Normalized reflected cavity signal measured with the photodiode (Thorlabs, DET10C).

into account the sidebands created by the frequency mixer. The coupling efficiency into the TEM_{00} mode and the losses inside the cavity also affect the visibility. The reason why the modulation depth is only dependent on the amplifier gain and cannot be changed otherwise is because each circuit element has to fulfill certain requirements in order to work properly and to not saturate. The precise requirements are specified in figure A.2. The visibility is rather modest, but by taking into account the losses inside the cavity and the current coupling efficiency of $c_{\mathrm{eff}} = (79.7 \pm 0.2)$ %, it is hardly improvable. Therefore, we decided to move forward with the PDH-lock.

The next step in order to achieve a stable lock is to create an error signal as described in section 2.5. For this purpose, the reflected cavity signal is forwarded to another frequency mixer (Mini Circuits, ZAD-8+, this time used for downconversion), in order to demodulate the signal with the frequency Ω' used for creating the sidebands (as shown in figure 3.3). The output signal from the mixer passes through a 1 MHz low-pass filter, that filters out the high modulation frequency, since we are only interested in the DC signal. This further leads to an error signal as presented in the theory about PDH locking (section 2.5). The error signal yields the sign about which way to move the frequency in order to be back on resonance again. A first result for the error signal is shown in figure 4.2. Here, the error signal presents the same features as the one in figure 2.6, namely peaks and dips above and below the noise floor, representing the direction of correction.
However, we still face the following issues: the SNR is very small (approximately 2:1), as

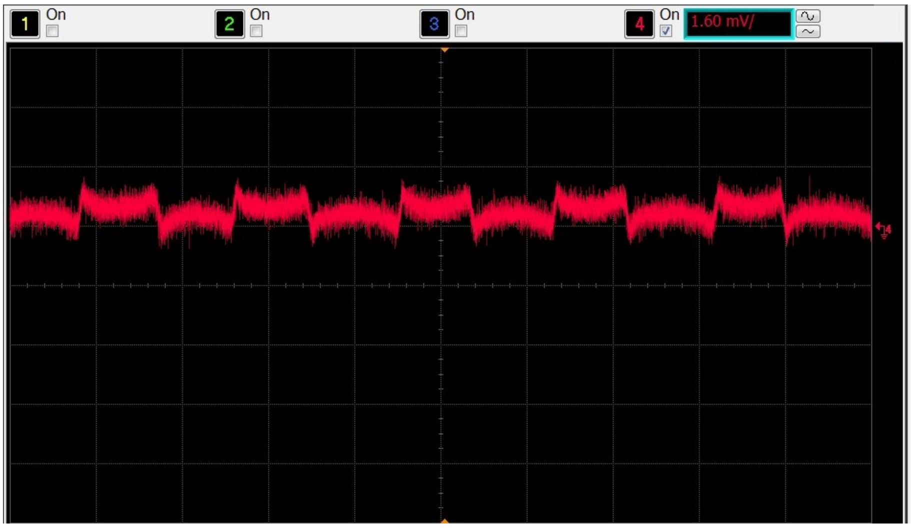

Figure 4.2.: Screenshot from the oscilloscope of the first result for the error signal resulting from the demodulated reflected cavity signal. The voltage per division (white rectangles) is 1.6 mV and zero is marked by a red arrow on the right edge.

we would expect from the earlier considerations described above. Furthermore, the signal has a slight offset and does not oscillate around zero. In addition, sometimes the signal does not repeat itself properly in time. We sometimes observe an error signal consisting only of peaks or only of dips, making the error signal unusable since it should yield both. Therefore, we introduce an offset and a phase shift to the demodulation sine wave in order to get a signal that yields a sign about the direction (oscillation around zero). Moreover, we introduce a phase at the MHz function generator creating the demodulation frequency Ω' for the mixer. This has the goal of counteracting the imbalance of peaks and dips. This approach worked for some time, but the phase needs to be adapted continuously. Also, the SNR stayed the same. In order to improve the SNR we try to amplify the signal with a self-built low noise amplifier. We expect this to improve the SNR, since the noise is at a different frequency as the signal. Since the amplifier gain is frequency dependent, this should have an impact on the SNR.

4.2. Improvement using an amplifier

We use a dual low-noise operational amplifier (Texas Instrument, ne5532a). In this context, dual means that the amplifier has two input and output ports, however, we only need one of them. We chose to use a non-inverting amplifier, such that the sign of the signal stays the same. The circuit is shown in figure 4.3.

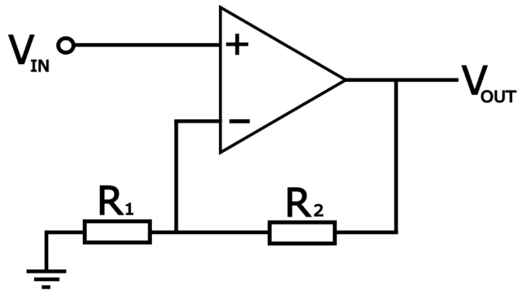

Figure 4.3.: Circuit of the non-inverting configuration of the amplifier. V_{IN} describes the input voltage that needs to be amplified. The amplification gain is dependent on the choice of resistors $R_{1,2}$. V_{OUT} is the amplified output signal.

The amplification gain g of the amplifier is given by the ratio of the two resistors (see figure 4.3)

$$g = 1 + \frac{R_2}{R_1} \tag{4.2}$$

In order to determine the optimal working conditions of the amplifier, we perform measurements of the SNR versus the input laser power for different amplification gains. We want to use the best possible SNR at an adequate laser power, which should not be too high to avoid heating effects. The resistors R_1 and R_2 are chosen such that g = [50, 100, 500], in order to cover a large range with large differences.

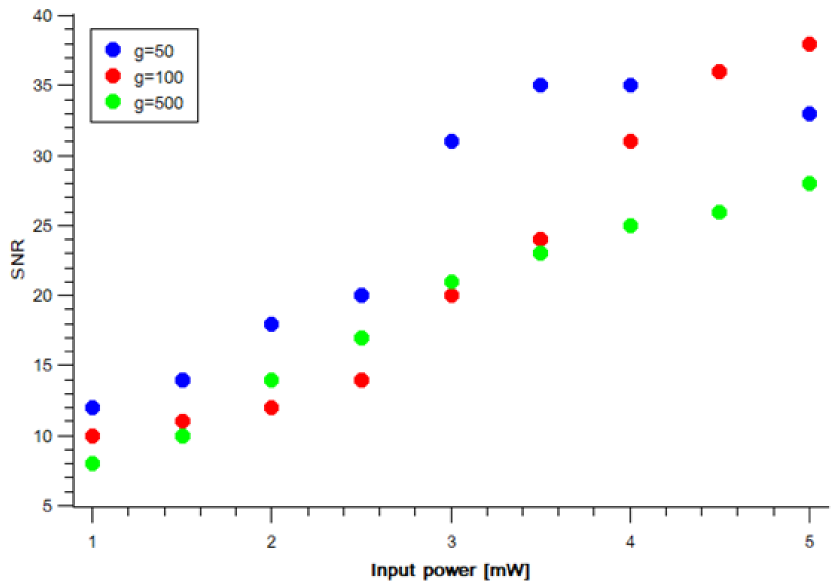

Figure 4.4.: SNR versus input laser power for different amplification gains.

The graph in figure 4.4 shows an example of SNR measurements as a function of the input power. From there, one can conclude that in general it is better to use higher input powers than lower ones. This is plausible, since the visibility always stays at the same percentage, while the power level is raised. However, in order to avoid heating effects and optical damage inside the cavity, we choose an input power of 3.5 mW for the locking scheme, where the SNR is still improved compared to without using an amplifier. In terms of g, the SNR is higher for relatively low amplifications. Figure 4.5 shows an example of the error signal under the conditions $g = 50$ and input power $P_{\text{in}} = 3.5$ mW.

It is important to note with respect to the data in figure 4.4 and 4.5 that

- the SNR was measured differently for the data presented in figure 4.4. Those values were determined by calculating the ratio of the root mean square (RMS) of the noise to the peak-to-peak voltage of the signal. This leads to an overestimation of the SNR. However, since the purpose of the data in figure 4.4 is to determine the best conditions for input power and amplification gain, this has no effect on the shape of the presented curves.

- figure 4.5 only shows an example error signal that was measured over a shorter integration period than the data for the SNR presented in figure 4.4. This also leads to artificially higher values of the SNR for the data in figure 4.4.

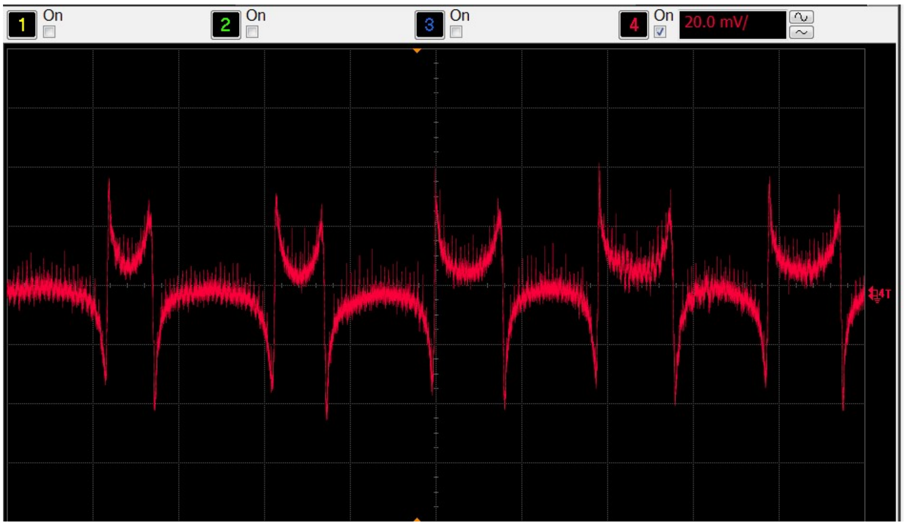

Figure 4.5.: Example for an amplified error signal for an input power of 3.5 mW and $g = 50$. The voltage per division is 20 mV.

This result has a sufficiently large SNR and we decided to process the signal and send it to our PID.

4.3. The PID

As already described in section 2.6, the PID consists of three different filters we can apply to our error signal. With the PID, the sideband frequency Ω created by the GHz function generator is supposed to follow the drifting cavity resonance mode. Using only the P and I part of the controller can already be sufficient. For this reason, we decide to neglect the derivative part (set $\tau_d = 0$). Therefore, we set the proportional value k_p and the integral value τ_i and choose a set point (which is 0). In the end, we want to implement a slow and a fast lock. For the fast lock, the output signal $\mathrm{PID_{out}(t)}$ is connected directly to the GHz function generator, that counteracts small deviations from the set point within the deviation window specified by the function generator. The $\mathrm{PID_{out}(t)}$ signal will have a certain amplitude we can set. The input to the GHz function generator acts as a frequency modulation where -1 to 1 V corresponds to some frequency range between 250 kHz and 1 MHz (this can be set on the function generator). However, the slow lock is supposed to counteract also larger deviations, which cannot directly be done by the function generator. For this purpose, we need to write programs that forward the $\mathrm{PID_{out}(t)}$ signal to the function generator to directly adjust its output frequency. Since it is not possible for the Red Pitaya to directly control the function generator, we wrote programs using Python that create a TCP/IP connection between the Red Pitaya and the lab computer. The lab computer is able to connect with the function generator and acts therefore as a mediator between Red Pitaya and function generator. A description of the corresponding python scripts can be found in the appendix B.1 for programs 1-4. By means of those scripts, we were able to stream the $\mathrm{PID}_{\mathrm{out}}(\mathrm{t})$ data from the Red Pitaya with the lab computer. The lab computer further converts the data to frequency values and sends them to the function generator via USB connection. The function generator will make according adjustments for the output frequency and therefore follow the resonance mode. The ideal case is that the laser will always stay on resonance with the cavity mode, which we would observe with the camera. However, each time we try to conduct the cavity lock, the mode still drifts away within only a few seconds. When we again had a look at the error signal, we found out that the signal shown in figure 4.5 was not reproducible. As already mentioned before, the phase of the signal has to be adjusted continuously in order to receive a proper error signal. Furthermore, as shown in figure 4.5, the noise might be too large, such that the set point for the PID cannot be distinguished from noise. Within the noise are several smaller peaks that could possibly lead to a wrong action of the PID. We conclude that the SNR of 2:1 of the unamplified error signal is still not good enough, resulting from the SNR of 3:1 of the reflected signal of the cavity. This is due to the distribution of the input power in all the sidebands we create with the EOM (see figure 3.5). Since not all of the sidebands and not even the carrier frequency are necessary, we decided to build a broadband filtering cavity that filters out all the frequencies that are not needed. This would then result into a higher visibility and a higher SNR of the reflected signal.

4.4. Building the filtering cavity

We first evaluate what properties the filtering cavity has to meet. Since the GHz function generator generates frequencies between Ω = 0.5 - 2.1 GHz, the filtering cavity linewidth should be significantly smaller than that, because otherwise it would not serve its purpose of filtering. On the other hand, it should be larger than the sideband frequency created by the frequency mixer, which is at 10 MHz. Therefore, the cavity linewidth is chosen to be $\approx$ 100 MHz. All frequencies outside the interval of 100 MHz would therefore be filtered out. The sidebands within this range will be slightly affected concerning the amplitude, but since the FWHM is at 100 MHz, the sidebands at $\pm$10 MHz should not be significantly affected. Furthermore, the cavity length should be tunable using a piezoelectric chip (Thorlabs, PA44M3KW) and sufficiently short, in order to make sure that the cavity is stable (see figure 3.1) and to achieve the desired linewidth of $\approx$ 100 MHz. The FSR of the cavity should not be too large either, since we need to scan with the piezo at least 1 FSR, which is hard to achieve if it is too large. The mirrors are chosen to have identical properties (concave, reflection coefficients $R_{1,2} = 0.99 \pm 0.002$, radii of curvature $r_{1,2} = 100$ mm and half-inch diameter $d = 12.7$ mm). Since there is no value for the transmission coefficients given in the specs, they are assumed to be $T_{1,2} = 1 - R_{1,2}$. A schematic of the filtering cavity is given in figure 4.6.
We insert the mirrors into two half-inch lens tubes that are glued to the piezo with a UV-glue. In this way, the mirrors can be placed very precisely to keep the uncertainty as low as possible. Also, it is a stable system, leading to less influence of vibrations. This system leads to a cavity length that is only determined by the piezo thickness $d_{\mathrm{piezo}} = 3.2$

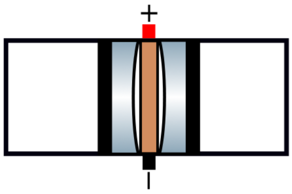

Figure 4.6.: Schematic of the filtering cavity. The mirrors (grey) are put into two lens tubes (white, transparent) which are glued to the piezo (brown). The + and - denote the electrodes of the piezo where a voltage is applied. The mirrors are fixed by retaining rings (black) that are screwed into the tubes.

mm and the radius of curvature of the mirrors $r_{1,2} = (100 \pm 0.1)$ mm, $L_{\text{filter}} = (3.6 \pm 0.2)$ mm. The FSR is $\Delta\nu_{\text{FSR}_{\text{filter}}} = (41.64 \pm 2.31)$ GHz, while the expected finesse is $\mathcal{F}_{\text{filter}} = 312 \pm 63$, leading to an expected linewidth of $\Delta\nu_{\text{filter}} = (133 \pm 28)$ MHz.

The filtering cavity is placed in the setup directly after the EOM, before the Faraday rotator. Figure 4.7 shows the illustration of the modified setup including the filtering cavity and figure 4.8 shows a photograph of the setup.
The fiber after the EOM is connected to a collimation package, such that the output beam is collimated. Since the reflected signal of the filtering cavity is not needed, a Faraday isolator is inserted before, which discards the reflected beam. Then the light passes through a lens and finally the filtering cavity. In order to choose the optimal focal length for the lens, the properties of the laser beam, such as the beam waist and Rayleigh length, have to be known. For this purpose, the beam diameter is measured using a razor blade placed on a translation stage and a photodiode measuring the transmitted power. This measurement was performed four times at different positions. Figure 4.9 shows an illustration of the measurement scheme. The corresponding measurement results can be found in the appendix tables A.5 - A.8 and in figure A.5.
From those results, the beam waist and its position are determined to be $w_0 = (0.38 \pm 0.02)$ mm and $z_0 = (4.51 \pm 32.4)$ mm (using programming scripts from B.2 2 and 3). Using formula 2.15, this corresponds to a comparatively large Rayleigh length of $z_R = 426 \pm 45$ mm, which is expected since the beam is supposed to be collimated. After some calculations (see scripts from B.2 1 and 4) we determine that the lens should ideally have a focal length of $f = (78.5 \pm 5)$ mm. The uncertainty results from an estimation of the uncertainties for the optical components taken into account for this calculation (thickness of the cavity mirrors, their radii of curvature etc.) as well as from w_0. Therefore, we choose a lens with $f = 75$ mm, since it has the closest matching standard focal length.

We scan the filtering cavity using a piezo stage that changes the cavity length. We need a voltage range that is able to scan at least 1 FSR of $\Delta\nu_{\text{FSR}_{\text{filter}}} = (41.64 \pm 2.31)$ GHz. From the data sheet of the piezo we estimate that (13.5 ± 0.5) V corresponds to 1 FSR. Another Red Pitaya is used to generate a low-noise DC voltage output signal that ranges

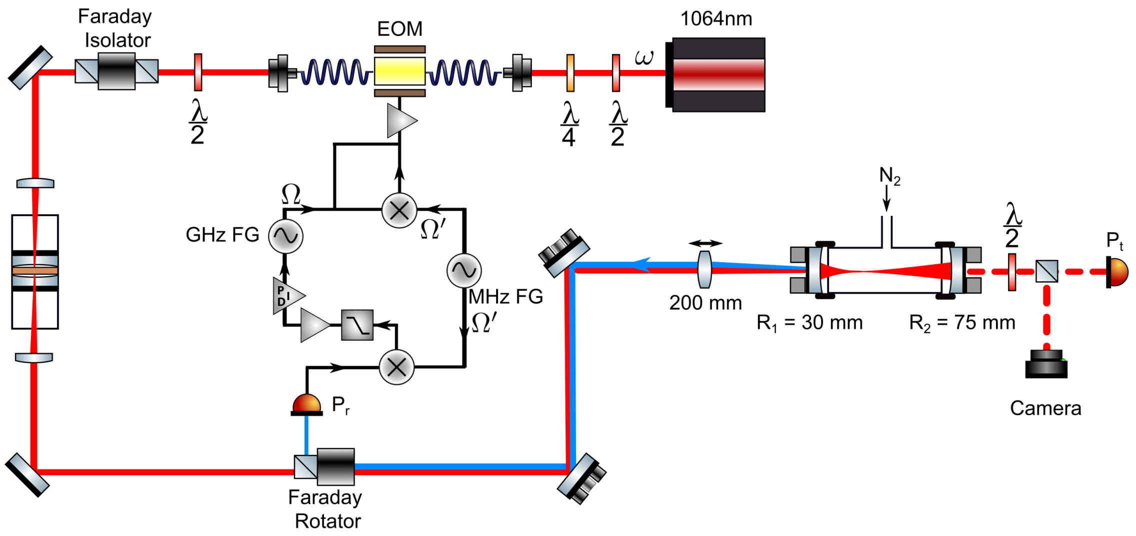

Figure 4.7.: Experimental setup for cavity lock. The beam enters the EOM, driven by the RIGOL function generator, in order to create sidebands. Then it passes through a faraday isolator before entering the filtering cavity. The transmitted light is processed to a Faraday isolator (such that the back reflected light from the second cavity may be used) and is finally coupled to the high-finesse cavity. The light that is transmitted is split up by a beam splitter such that it can be detected by both a photodiode and a camera. The reflected beam is detected by a photodiode and forwarded to a frequency mixer in order to create an error signal. This error signal passes through a low pass filter and an amplifier before entering the Red Pitaya (PID), that sends the modulated signal back to the RIGOL function generator to lock the cavity.

from 0 to 2 V. This Red Pitaya was modified such that it produces a low-noise output, compared to unmodified Red Pitayas. The modification has been done by removing one resistor that leads to an offset in the output, such that the output usually ranges from -1 to 1 V. However, this offset also introduces noise [48]. Before removing the resistor, the peak-to-peak voltage of the background noise was at $V_{\text{noise}} = (6.23{\pm}0.02)$ mV (measured with the oscilloscope). The background noise of the modified Red Pitaya is at $V_{\text{noise}} = (1.23{\pm}0.05)$ mV. This output signal is connected to the piezo drive (PiezoDrive, PDu150), which amplifies the signal with an amplification gain of 20. We need a noise as low as possible, since the smallest steps the Red Pitaya can make are 1 mV steps. After the piezo drive, this will correspond to 20 mV steps at the piezo. In frequency, 20 mV already correspond to a step of $(61.7{\pm}4.1)$ MHz, which is approximately half a linewidth. If the noise would be larger, we would observe a scanning effect since the peak-to-peak voltage of the noise would be amplified as well. A python script (see appendix B.1 4) controls the Red Pitaya output and is able to scan the cavity over a range of 0 - 40 V (0 - 2 V of

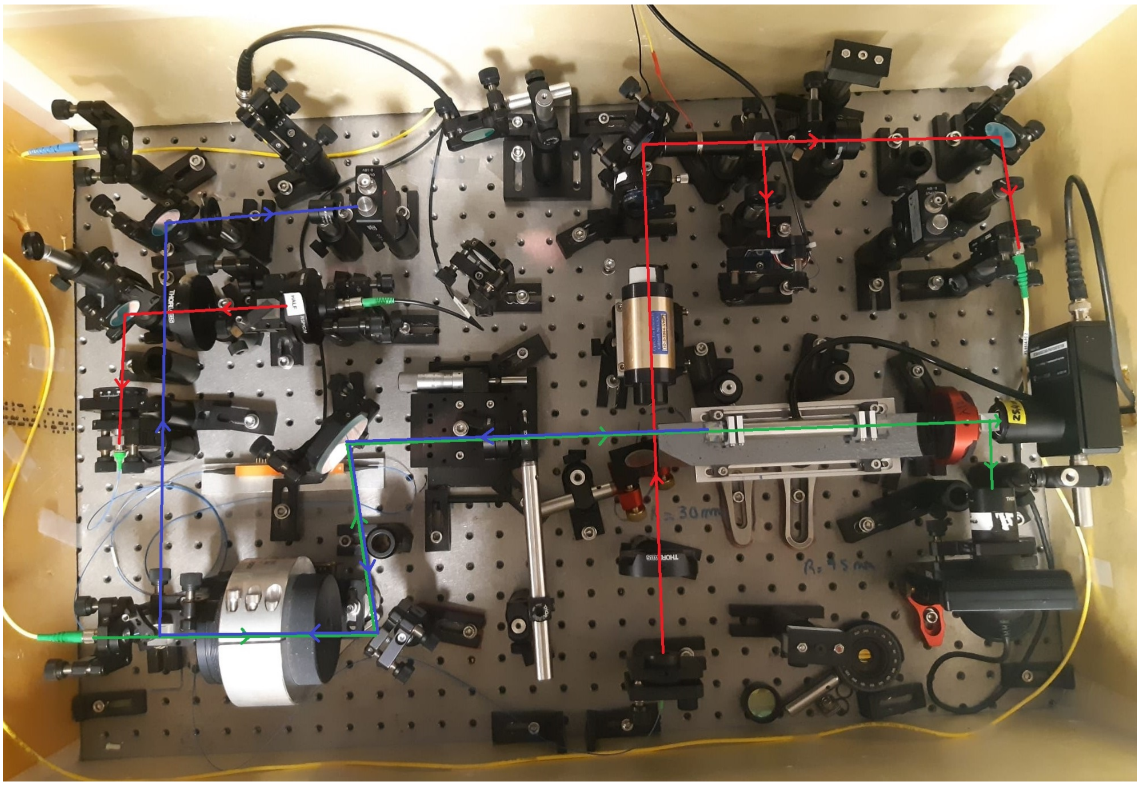

Figure 4.8.: Real picture of the setup. The red line in the left part of the photo is part of the laser beam coming from the Mephisto laser. The beam goes through a fiber to the EOM (orange, left) and from there to the filtering cavity (on the right side). After being coupled to the fiber after the filtering cavity, the laser beam is labeled with a green line. It goes through the high finesse cavity where it is detected by both a camera and a photodiode. The blue line marks the beam that is reflected from the high finesse cavity.

the Red Pitaya after amplification). Since one FSR corresponds to a range of (13.5±0.5) V, we are therefore able to scan at least two FSR, even though one FSR would have been sufficient. The transmitted light is split at a PBS in order to detect it by both a camera (Basetech Classic BS-WC-01 Webcam) and a photodiode (New Focus, model 1623). We use the camera to monitor the TEM modes corresponding to the power measured with the photodiode. Once the TEM_{00} mode is found, the coupling efficiency is maximized. We need to couple into the TEM_{00} mode as well as possible in order to keep the power loss as low as possible. In table A.3 in the appendix, we provide the measurement data for the coupling efficiency. Since there exist two TEM_{00} within one FSR, both are taken into account. The most likely explanation for seeing two TEM_{00} modes is that the cavity is birefringent such that the two principal axes defined by the cavity exhibit a slightly different FSR. We found $c_{\text{eff}} = (96.4 \pm 0.1)$ %. Since we assume $T_{1,2} = 1 - R_{1,2}$, all of

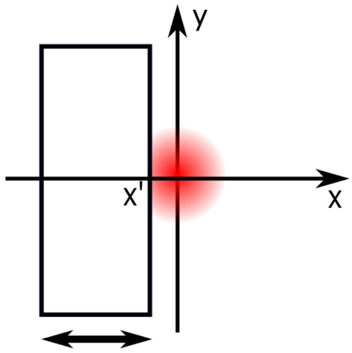

Figure 4.9.: Beam waist measurement with a razor blade.

the input power is supposed to be transmitted when being on resonance ($I_t = I_{in}$). This means that the transmitted power is only dependent on c_{eff}. However, a measurement with the power meter yields that only (58.7±2.5) % of the input power are transmitted. Since we can only be on resonance with one of the two existing TEM_{00} modes, the general calculation of how much light is coupled into the TEM_{00} is still correct, but is not applicable to the transmitted intensity. Since the two existing TEM_{00} modes have different transmitted powers, c_{eff} is recalculated by taking into account only the higher power TEM_{00} mode. This results into $c_{eff} = (71.6\pm0.3)$ %. Since c_{eff} is still measured to be higher than (58.7±2.5) %, this means that there is either more absorption in the cavity mirrors than expected or that the mirrors are also affected by the humidity in the lab, as the mirrors used for the high-finesse cavity. The experimental data in table A.3 show that the coupling efficiency cannot be further improved, since the (96.4 ± 0.1) % coupling into the two TEM_{00} modes is already close to 100 %. Therefore, we continue and perform measurements with the underlying transmitted power, as will be described in the following.

The next thing to do is to measure the linewidth of the filtering cavity in order to confirm that the mirrors we are using suit our purpose. The expected value of the cavity linewidth is $\Delta\nu_{filter} = (133\pm28)$ MHz. Figure 4.10 shows the measured data for determining the linewidth of the filtering cavity. We use the sidebands generated by the GHz function generator to calibrate the x-axis. Since the sidebands are created at a value we can choose at the function generator, the x-axis that was originally in units of time can be converted to frequency. This can be done since the distance between center peak and sideband peak in time are known to correspond to a certain value in frequency. After this conversion, a Lorentzian fit to the data will yield a direct measure for the linewidth. The measurement is repeated four times. The measurement result yields a linewidth of $\Delta\nu_{filter} = (86\pm7)$ MHz. This is less than expected compared to the expected linewidth of (133±28) MHz, but since the reflection coefficients of the mirrors are given by $R_{1,2} = 0.99\pm0.002$, it might be that at least one of the mirrors is an outlier and has an even lower reflection coefficient. Nonetheless, the linewidth is sufficient for the purpose of filtering, because it is still much

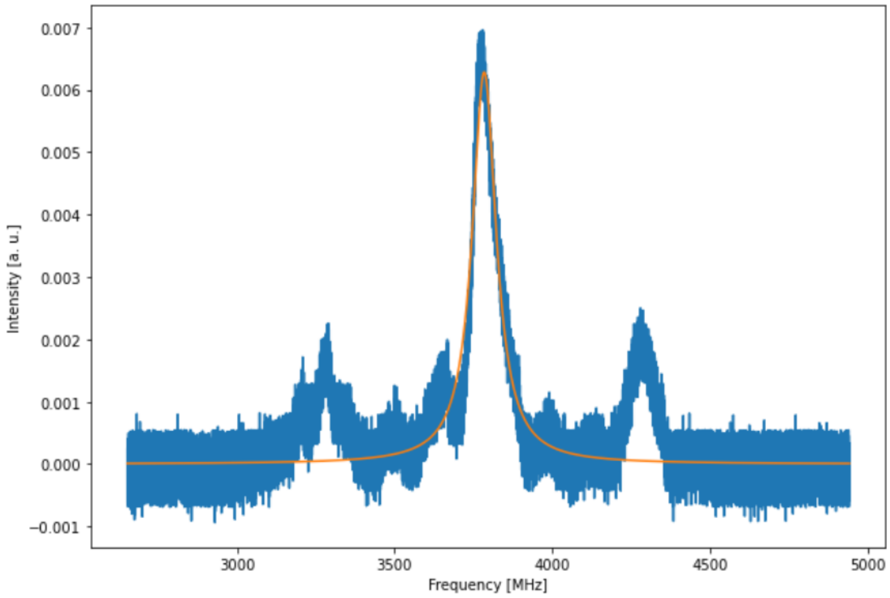

Figure 4.10.: Example for linewidth measurement of the filtering cavity with sidebands at ±500 MHz and Lorentzian fit (orange line) for the transmitted signal.

larger than the distance between one sideband and the sidebands created by the MHz function generator, which is $\Omega' = 10$ MHz. As can be seen in figure 4.7 and 4.8, the beam first has to pass another lens in order to become collimated again. Ideally, this lens should have had the same focal length as the lens used for coupling into the cavity ($f = 75$ mm), to match the same collimation package as at the input of the cavity. However, since the same lens was not available at the time when we built the setup, the lens we use after the filtering cavity has a focal length of $f = 100$ mm. So far we have not replaced the lens because it would only result in a minor increase of input power for the high-finesse cavity. We can compensate for that loss in power by increasing the laser power. After passing this lens, the beam is directed to the collimation package and coupled into a single mode fiber. Probably due to the choice of the lens, a coupling efficiency of only $c_{\text{eff}} = (60 \pm 1)$ % is reached. The output of that single-mode fiber is then connected to a fiber collimator and coupled into the high-finesse cavity as shown in the green path in figure 4.8. The resulting beam then only contains three different frequencies ($\omega + \Omega$, $\omega + \Omega - \Omega'$ and $\omega + \Omega + \Omega'$), as shown in figure 4.11.

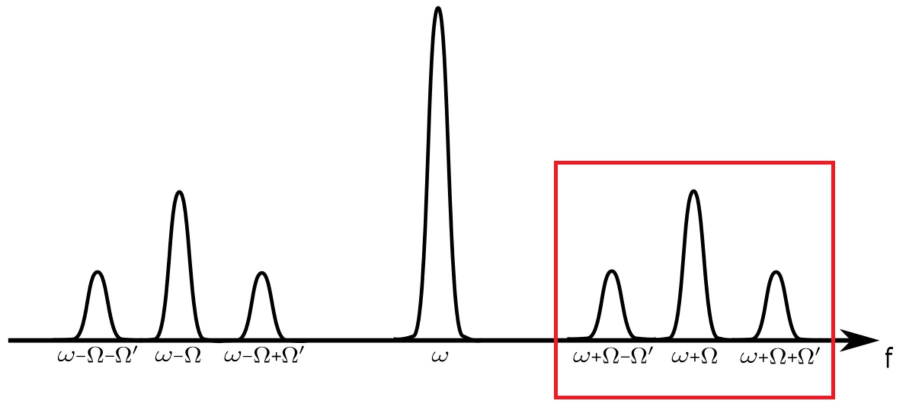

Figure 4.11.: Frequencies created by the EOM. The frequencies within the red square are getting through the filtering cavity, the rest is filtered out. Note that this is a simplified illustration and that the x- and y-axis are not true to scale. The sidebands at $\omega + \Omega - \Omega'$ and $\omega + \Omega + \Omega'$ will be slightly diminished by the finite linewidth of the filtering cavity.

4.5. Results with the filtering cavity

In this section we explain how the beam exiting the filtering cavity is coupled again to the high-finesse cavity again. For this purpose, a calibration curve that follows the filtering cavity resonance mode while scanning through the high-finesse cavity is needed. To do that, we are on resonance of the filtering cavity with one sideband and then change the sideband frequency. This has the effect of being not longer perfectly on resonance, depending on how much we changed the sideband frequency. Then we measure by how much the voltage that drives the piezo has to be changed in order to be back on resonance. The result is shown in figure 4.12.

We fit the experimental data using a linear fit that gives $a = 2.34{\times}10^{-11}$ V/Hz can be determined. Using the python scripts (appendix B.1 3 and 4) we are now able to scan through the high-finesse cavity and simultaneously stay on resonance with the filtering cavity. Since the filtering cavity has a large linewidth ($\Delta\nu_{\text{filter}} = (86\pm7)$ MHz) compared to the high-finesse cavity ($\Delta\nu = (25\pm1)$ kHz), the mode drifts very slowly, meaning that we are able to stay on resonance with the filtering cavity for several minutes without any additional stabilization mechanisms.

Once the TEM_{00} mode is identified using a camera (PlayStation Eye), the coupling efficiency can be improved, such that the photodiodes are able to detect signals for transmission and reflection. With the photodiode in reflection, we are able to measure the visibility improved by the filtering cavity. The experimental data are shown in fig. 4.13.

Using a Lorentzian fit, we extract a visibility of $\mathcal{V} = (16\pm1)$ %, improving the visibility by a factor 3 compared to the visibility measured before $\mathcal{V}_{\text{old}} = (5\pm0.5)$ %. The uncertainty

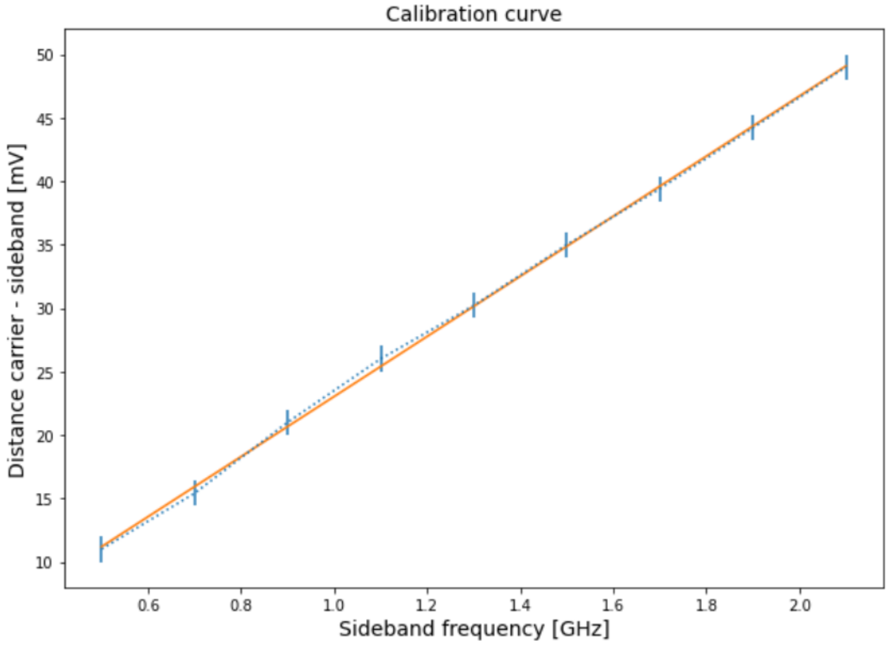

Figure 4.12.: Calibration curve between sideband frequency and voltage that drives the piezo. The x-axis shows the frequency as generated by the GHz function generator. The y-axis shows the distance between carrier and sideband set by the Red Pitaya that drives the piezo. The blue dotted line shows the experimental data, while the orange line is a linear fit using y $= a$x $+ b$. x and y correspond to the data on the x-axis and y-axis in the plot. The fit yields the calibration parameter $a = 2.34\times10^{-11}$ V/Hz.

is again estimated from the oscilloscope. The SNR is around 6:1, which is also improved compared to the SNR without filtering cavity, which was around 3:1. From the Lorentzian fit, the linewidth can again be estimated, giving $\Delta\nu = (24.9\pm1.4)$ kHz. This still coincides with what was measured in 3.8b, meaning that our solution of using nitrogen against the humidity is still valid. The coupling efficiency is measured to be $\approx (74.9\pm1.1)$ % (see table A.4). We generate an error signal using the same mixer as without filtering cavity (Mini Circuits, ZAD -8+) and let it pass through a low-pass filter (1 MHz). The result is shown in figure 4.14. It shows an error signal without any amplification. The SNR is improved up to approximately 4:1 compared to without filtering cavity, which was around 2:1. Even without amplification, this might be sufficient for the locking procedure. This time the peaks and dips of the error signal are clearly standing out from the noise, giving a clear sign about the direction in which we have to modify the frequency of the GHz function generator. This error signal is a good foundation for future work, which will contain the locking. Due to time constrains, the success of the lock of the cavity is not described in this thesis.

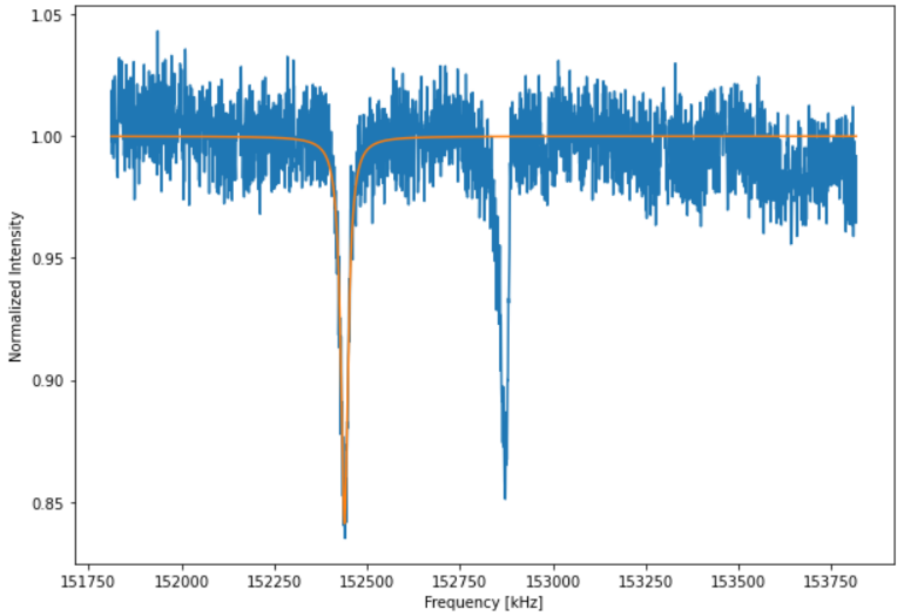

Figure 4.13.: Reflected signal of the high-finesse cavity with filtered input beam. The blue line shows the original signal and the orange line a Lorentzian fit.

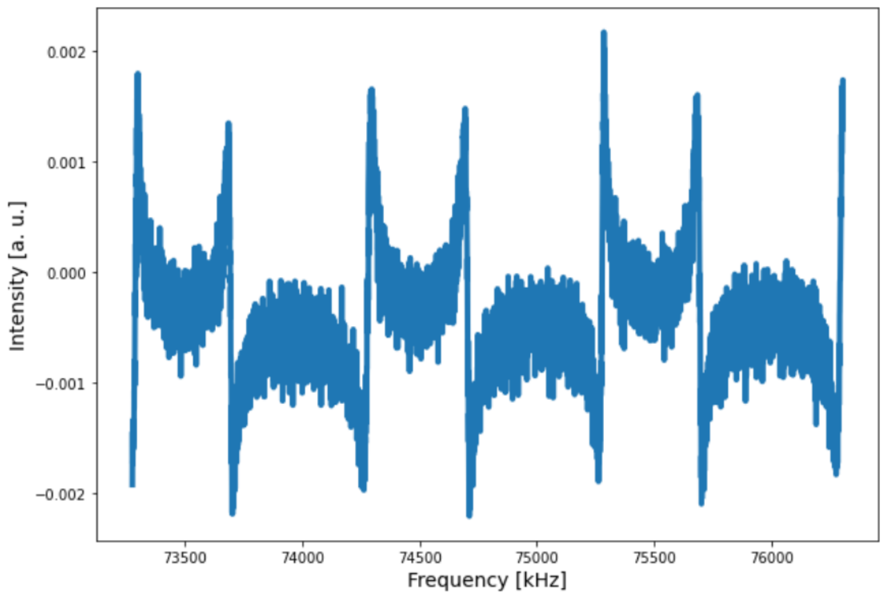

Figure 4.14.: Error signal with improved SNR compared to without filtering cavity resulting from the improved visibility of the reflected cavity signal.

5. Conclusion and Outlook

In this thesis, the aim was to lock the Mephisto laser to the resonance mode of the high-finesse cavity prototype for MAQRO. This has to be achieved in order to obtain a stable signal transmitted through the cavity. By improving the reflected cavity signal needed for the PDH locking, we achieved a good basis for conducting the lock. However, due to lack of time, the locking itself was not achieved. Starting from characterizing the cavity until the attempts on improving the reflected cavity signal, there were many challenges that had to be overcome. In this final chapter, we summarize the working process, analyze the reasons why locking the cavity did not work, propose possible solutions and discuss the next steps.

5.1. Visibility and SNR of the reflected high-finesse cavity signal

One main challenge was to understand the reasons for the modest visibility of our reflected high-finesse cavity signal. At the beginning, we assumed a transmission coefficient of the mirrors of $T_{1,2} = 1$ - $R_{1,2}$. This would lead to a theoretical visibility of the reflection dip of 100 % that only further depends on the coupling efficiency and power distribution into the sidebands. Since at the beginning we only measured $\mathcal{V} \approx 2$ %, we spent a lot of time on improving the coupling efficiency. This was a challenge due to the narrow linewidth of the cavity leading to a strong drift (up to a few MHz per second). By doing so, the visibility was improved up to $\mathcal{V} = (5 \pm 0.5)$ %. We concluded that the coupling efficiency is good enough to receive a higher visibility than that. Only then we realized that the maximum visibility (without modulation) is expected to be $\mathcal{V} = 25$ %, due to comparatively low transmission coefficients of the mirrors, that were actually given by the specifications. This finally explained the low visibility we observed, by also taking into account the power distribution into all sidebands. Nonetheless, we pushed forward to implement the locking scheme of the cavity.

5.2. The locking scheme

We continued with the implementation of the PDH-locking technique. After producing an error signal with SNR 2:1, we wanted to amplify the signal in order to have more visible signs. This should work since the noise stems from different frequencies than the signal. The amplifier has different gains for different frequencies, leading to the hope that it would amplify the signal stronger than the noise. However, the amplified signal was not reproducible. The shape of the error signal was sometimes unusable, since it showed signs in only positive or negative direction. This might result from the phase that had to be adjusted at the MHz function generator for each measurement. After adjusting the phase such that the error signal shows the desired shape, it quickly changed again. In this case, we had to adjust the phase again.

Another challenge that had to be faced was to establish a TCP/IP connection between the lab computer and the Red Pitaya, that is fast enough to suit our purpose. If the overall communication between Red Pitaya and function generator was too slow, the counteractions from the PID to any disturbances could not be adapted fast enough. The $\mathrm{PID_{out}}(t)$ signal had to be read out and converted in frequency such that the GHz function generator can adjust its output frequency accordingly. Once the TCP/IP connection was established, we had to write a program that is able to control the Red Pitaya such that we can directly read out the data and forward them to the function generator. The programs running on the Red Pitaya are written in C, while our programs for the TCP/IP connection are written in Python. There already existed Python programs to control the Red Pitaya remotely and therefore to stream the data (given by the module "Lock-in + PID" by Marcelo Luda [40]), but those were operating too slowly. Therefore, we had to write and call the functions directly in and from the C programs running on the Red Pitaya and optimize them such that they are fast enough (maximum 10 ms for the overall communication process Red Pitaya - lab computer - function generator). Once we tried to apply our PID controller on a proper error signal, it still did not work. This might result from the noise that is still large compared to without amplification. When trying to lock without any amplification at all, the signs of the error signal were probably too buried in noise in order to apply a PID, which needs a certain set point. If the set point is almost the same as the disturbance, then the PID can hardly produce a counteracting signal. Sometimes we assumed to observe a few stable seconds, but this might have been coincidentally.

5.3. Improvement of visibility and SNR

We concluded that the underlying visibility of the reflected cavity signal, and therefore the SNR, are not high enough in order to conduct the PID. Since there is a lot of the cavity input power distributed into all the sidebands, we considered it necessary to implement a filtering cavity after the EOM. This filters out all the unnecessary frequencies, since we only need one sideband at $\omega \pm \Omega$ and two additional sidebands for PHD locking at $\omega \pm \Omega \pm \Omega'$. The choice of the properties the cavity mirrors should have was given by the fact that Ω = 0.5 - 2.1 GHz and Ω' = 10 MHz. Therefore, we had to choose the properties such that the resulting cavity linewidth is significantly larger than Ω' but smaller than Ω. However, at the beginning we ordered mirrors that had no specified transmission and absorption coefficients, so we assumed the absorption to be low. Once the mirrors were implemented into the setup, the coupling efficiency was maximized and still we observed almost no transmission. After a long time of improving the coupling and realigning the laser beam, the transmission of only one mirror was measured to be very low. We concluded that the absorption coefficient is almost $A_{1,2} \approx 1 - R_{1,2}$ for both mirrors. Finally, we ordered mirrors that fit our purpose (the one described in chapter 4.4). The results presented in chapter 4.5 show that the filtering cavity improved both the visibility and the SNR of the reflected cavity signal.

5.4. Outlook

With the new results for visibility and SNR, the next step would be to try the locking scheme again as described in chapter 4 without amplifier. The signs of the error signal are distinct enough from the noise, such that it should be feasible to successfully implement the PDH lock. The work presented in this thesis laid the basis for the anticipated future success in realizing a stable lock of an individual GHz sideband to the MAQRO prototype cavity. The SNR of the error signal could be further improved by increasing the input power of the high-finesse cavity, but since we want to avoid heating effects and optical damage within the cavity, it has to be kept reasonably low, which is few mW. What is still missing in order to make the lock work is the python script that enables a TCP/IP connection between two Red Pitayas at the same time, since there is one more Red Pitaya compared to without filtering cavity, that drives the piezo and has to be adjusted according to the data received from the second Red Pitaya for the lock (as described in section 4.5).

After the lock is working, there will be a stable beam transmitted through the high-finesse cavity. This will be used to glue further mirrors to the optical bench. Those mirrors will be used to couple the light coming from the laser through a fiber into the cavity, as it will be done in space. Figure 5.1 shows a model of the optical bench and all components glued to it as it will look like in the future. After the precise work of gluing all components to the optical bench, the setup will be placed in a cryogenic environment in order to test the suitability of the cavity design to operate successfully at cryogenic temperatures. To additionally demonstrate the space-readiness of our cavity prototype, we anticipate that the cavity will be operated continuously during many thermal cycles of cooling and heating. Additional future tests may be performed to further confirm the space-readiness of our prototype (shakers, operation in a drop tower, operation on an in-orbit-demonstrator, shock tests).

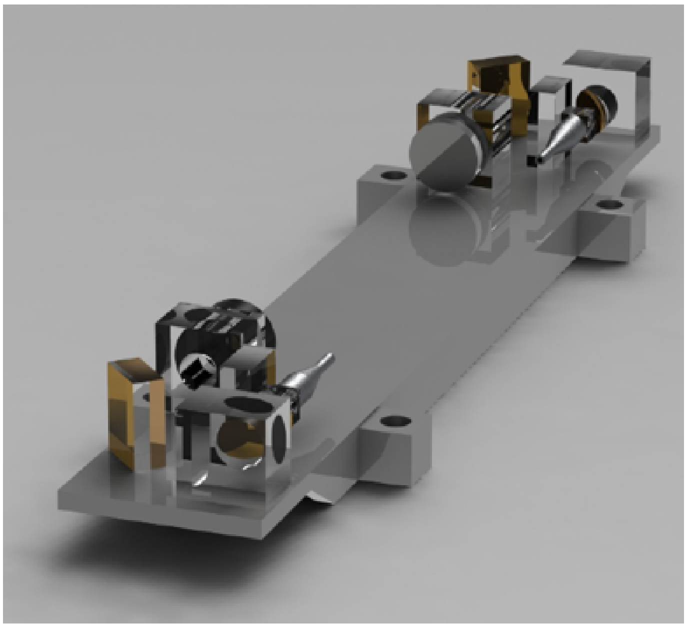

Figure 5.1.: A model of the optical bench with cavity mirrors and all optical components necessary to couple the laser into the cavity in space. The laser will come from one fiber and will be reflected around the corner in order to couple into the cavity. On the other end, the light transmitted through the cavity will be fiber coupled and detected. The 3D model was created by Rainer Kaltenbaek.

Bibliography

1. Kaltenbaek, R. *et al. MAQRO – BPS 2023 Research Campaign Whitepaper* 2022. arXiv: `2202.01535 [quant-ph]`.
2. Kaltenbaek, R. *et al.* Macroscopic quantum resonators (MAQRO): 2015 Update. *EPJ Quantum Technology* **3,** 5 (2016).
3. Kaltenbaek, R. *et al.* Macroscopic quantum resonators (MAQRO). *Experimental Astronomy* **34,** 123–164 (2012).
4. Hechenblaikner, G. *et al.* How cold can you get in space? Quantum physics at cryogenic temperatures in space. *New Journal of Physics* **16,** 013058 (2014).
5. Pilan Zanoni, A. *et al.* Thermal performance of a radiatively cooled system for quantum optomechanical experiments in space. *Applied Thermal Engineering* **107,** 689–699 (2016).
6. Drever, R. W. P. *et al.* Laser Phase and Frequency Stabilization Using an Optical Resonator. *Applied Physics B* **31,** 97–105 (1983).
7. Black, E. An introduction to Pound–Drever–Hall laser frequency stabilization. *American Journal of Physics* **69,** 79–87 (2001).
8. Fein, Y. *et al.* Quantum superposition of molecules beyond 25 kDa. *Nature Physics* **15,** 1242–1245 (2019).
9. Kaltenbaek, R. *et al. MQES Macroscopic quantum experiments in space using massive mechanical resonators (Po P5401000400)* (University, 2013).
10. Voirin, T. CDF Study Report: QPPF - Assessment of a Quantum Physics Payload Platform. *ESA* **CDF-183(C),** 1–272 (2018).
11. Stickler, B. *et al.* Probing macroscopic quantum superpositions with nanorotors. *New Journal of Physics* **20,** 122001 (2018).
12. Carney, D. *et al.* Mechanical quantum sensing in the search for dark matter. *Quantum Science and Technology* **6,** 024002 (2021).
13. Afek, G. *et al.* Coherent scattering of low mass dark matter from optically trapped sensors. *Physical Review Letters* **128,** 101301 (2022).
14. Riedel, C. J. Direct detection of classically undetectable dark matter through quantum decoherence. *Physical Review D* **88,** 116005 (2013).
15. Riedel, C. J. Decoherence from classically undetectable sources: Standard quantum limit for diffusion. *Physical Review A* **92,** 010101 (2015).

16. Riedel, C. J. & Yavin, I. Decoherence as a way to measure extremely soft collisions with dark matter. *Physical Review D* **96,** 023007 (2017).

17. Kaltenbaek, R. Feasibility considerations for free-fall tests of gravitational decoherence. *AVS Quantum Science* **4,** 015604 (2021).

18. Schlosshauer, M. *Decoherence: and the Quantum-To-Classical Transition* (Springer Verlag, 2007).

19. Joos, E. & Zeh, H. D. The emergence of classical properties through interaction with the environment. *Zeitschrift für Physik B Condensed Matter* **59,** 223–243 (1985).

20. Bateman, J. *et al.* Near-field interferometry of a free-falling nanoparticle from a point-like source. *Nature Communications* **5,** 4788 (2014).

21. Arndt, M. *et al.* Wave–particle duality of C_{60} molecules. *Nature* **401,** 680–682 (1999).

22. Nimmrichter, S. *et al.* Concept of an ionizing time-domain matter-wave interferometer. *New Journal of Physics* **13,** 075002 (2011).

23. Kiesel, N. *et al.* Cavity cooling of an optically levitated submicron particle. *Proceedings of the National Academy of Sciences* **110,** 14180–14185 (2013).

24. Kaltenbaek, R. & Aspelmeyer, M. Optomechanical Schrödinger Cats – a Case for Space. *"Erwin Schrödinger – 50 Years After",* 123–132 (2013).

25. Neuman, K. & Block, S. Optical trapping. *Review of scientific instruments* **75,** 2787–2809 (2004).

26. Delić, U. *Cavity cooling by coherent scattering of a levitated nanosphere in vacuum* PhD thesis (University of Vienna, 2019).

27. Riccardi, M. & Martin, O. Electromagnetic Forces and Torques: From Dielectrophoresis to Optical Tweezers. *Chemical Reviews* **123,** 1680–1711 (2023).

28. Bohren, C. & Huffman, D. *Absorption and Scattering of Light by Small Particles* (Wiley, 1998).

29. Bustamante, C. *et al.* Optical tweezers in single-molecule biophysics. *Nature Reviews Methods Primers* **1,** 25 (2021).

30. Yariv, A. *Optical Electronics* 4th ed. (Oxford University Press, 1991).

31. Hodgson, N. & Weber, H. *Laser Resonators and Beam Propagation* 2nd ed. (Springer Verlag, 2005).

32. Meschede, D. *Optics, Light, and Lasers. The Practical Approach to Modern Aspects of Photonics and Laser Physics* 3rd ed. (Wiley-VCH, 2017).

33. Paschotta, R. *Gaussian Beams* `https://www.rp-photonics.com/gaussian_beams.html`. Accessed: 06-2023.

34. Paschotta, R. *Resonator Modes* `https://www.rp-photonics.com/resonator_modes.html`. Accessed: 06-2023.

35. Paschotta, R. *Hermite–Gaussian Modes* `https://www.rp-photonics.com/hermite_gaussian_modes.html`. Accessed: 06-2023.

36. Pampaloni, F. & Enderlein, J. *Gaussian, Hermite-Gaussian, and Laguerre-Gaussian beams: A primer* 2004. arXiv: physics/0410021 [physics.optics].

37. Forget, S. *Hermite-Gaussian Modes* http://www.optique-ingenieur.org/en/courses/OPI_ang_M01_C03/co/OPI_ang_M01_C03_web.html. Accessed: 08-2023.

38. *AN002: Pound-Drever-Hall locking with the FSC* https://www.moglabs.com/support/appnotes/an002-pdh-r2.pdf. Accessed: 07-2023.

39. Johnson, M. & Moradi, M. *PID Control: New Identification and Design Methods* (Springer Verlag, 2005).

40. Luda, M. *et al.* Compact embedded device for lock-in measurements and experiment active control. *Review of scientific instruments* **90,** 023106 (2019).

41. https://redpitaya.com/. Accessed: 07-2023.

42. Kaltenbaek, R. *Photonics II - Lectures* (http://maqro-mission.org/wp-content/uploads/2020/06/photonics_II_Kaltenbaek_2020_lecture_notes_collection.pdf, 2020).

43. Boyd, R. *Nonlinear Optics* 3rd ed. (Academic Press, 2008).

44. Bond, C. *et al.* Interferometer techniques for gravitational-wave detection. *Living Reviews in Relativity* **19,** 3 (2016).

45. Hodgson, N. & Weber, H. *Optical Resonators: Fundamentals, advanced concepts and applications* (Springer Verlag, 1997).

46. Marki, F. & Marki, C. *Mixer Basics Primer: A Tutorial for RF Microwave Mixers* (Marki Microwave, Inc., 2010).

47. Della Valle, F. *et al.* Extremely long decay time optical cavity. *Optics Express* **22,** 11570–11577 (2014).

48. *Red Pitaya DAC performance* https://ln1985blog.wordpress.com/2016/02/07/red-pitaya-dac-performance/. Accessed: 08-2023.

A. Appendix

TEM_{nm} mode	Maximum voltage [mV]	Frequency [GHz]
30	4.45 ± 0.05	1.412
20	7.0 ± 0.1	1.365
02	7.0 ± 0.1	1.364
40	4.7 ± 0.1	1.114
04	4.7 ± 0.1	1.112
00	125 ± 1	0.792
10	12.4 ± 0.1	0.497

Table A.1.: Measurement of improved coupling efficiency c_{eff} for the high-finesse cavity. The maximum voltage was measured by the photodiode connected to an oscilloscope (Keysight, DSO9064A). It gives the maximum transmitted power for each occurring mode. The uncertainty was estimated from the oscilloscope. The result is $c_{\text{eff}} = 0.797 \pm 0.002$, calculated using equation 3.8

Level (dBm)	Diffraction efficiency (±5 %)
5	5
10	14
15	34
20	40

Table A.2.: The level was set on the RIGOL function generator that drives the EOM. The diffraction efficiency values are for one sideband. They were calculated by the ratio of the measured peak height at its maximum value to the input power. The peaks were measured using the spectrum analyzer of our oscilloscope. The uncertainty was estimated from the oscilloscope.

Figure A.1.: Frequency dependence of the gain of the amplifier before the EOM using a Network Analyzer (Keysight, PNA-L Network Analyzer N5232A). Between 1 GHz and 2.1 GHz (latter is the upper limit of the RIGOL function generator) the gain is $g \approx 30$ dB. At 500 MHz, $g \approx 20$ dB.

TEM$_{nm}$ mode	Maximum voltage [mV]
00	4950 ± 20
10	120 ± 5
LG 01	122 ± 5
LG 05	5 ± 1
LG 03	13 ± 1
LG 04	7.5 ± 1
LG 06	4.1 ± 1
00	1800 ± 20
00	5200 ± 20

Table A.3.: Measurement of the coupling efficiency of the filtering cavity. The measurement is conducted with an impedance of 10 kΩ on the photodiode in order to measure more defined peaks and therefore a more precise voltage. Since the coupling efficiency is only calculated as a ratio of intensities (see formula 3.8), we may use a higher termination than 50 Ω, leading to a longer response time of the photodiode. This is only possible if the signal is not further processed. The maximum voltage was measured with the oscilloscope. It gives the maximum transmitted power for each occurring mode. The dark noise for 10 kΩ on the oscilloscope is $V_{dark} = 1.66$ mV. The uncertainties were estimated from the oscilloscope. In this measurement, we also observe symmetric ring-shaped modes, so-called Laguerre-Gaussian modes. For example, a Laguerre-Gaussian 01 mode with one center point and only one ring around is referred to as "LG 01". There are three TEM$_{00}$ modes found, the first and the last being the same after one FSR. This means that there are two TEM$_{00}$ modes found within one FSR, probably belonging to two different polarizations. The coupling efficiency is calculated by assuming the TEM$_{00}$ mode to be the sum of both. In this case, the result is $c_{\mathrm{eff}} = 0.964 \pm 0.001$, calculated using equation 3.8.

TEM$_{nm}$ mode	Maximum voltage [mV]	Frequency [GHz]
50	2.3 $\pm$ 0.1	1.908
05	2.3 $\pm$ 0.1	1.907
04	15 $\pm$ 1	1.588
40	15 $\pm$ 1	1.587
03	5 $\pm$ 1	1.290
30	8 $\pm$ 1	1.289
20	8 $\pm$ 1	0.980
02	6 $\pm$ 1	0.979
01	8 $\pm$ 1	0.669
00	150 $\pm$ 5	0.373
00 (sb)	16 $\pm$ 1	0.380

Table A.4.: Measurement of coupling efficiency c_{eff} for the high-finesse cavity with filtering cavity. The maximum voltage was measured by the photodiode connected to the oscilloscope. It gives the maximum transmitted power for each occurring mode. The uncertainty was estimated from the oscilloscope. Since some of the power is distributed into the sidebands, c_{eff} is calculated by adding the TEM$_{00}$ sideband mode (marked by "sb") to the TEM$_{00}$ principal mode. The result is $c_{\text{eff}} = 0.749 \pm 0.011$, calculated using equation 3.8.

Position razor blade [mm]	Power [mW]	Uncertainty of Power [mW]
0	6.25	0.1
0.1	6.25	0.1
0.2	6.25	0.1
0.3	6.28	0.1
0.4	6.28	0.1
0.5	6.28	0.1
0.6	6.28	0.1
0.7	6.3	0.1
0.8	6.3	0.1
1.1	6.31	0.1
1.4	6.31	0.1
1.7	6.32	0.1
2	6.33	0.1
2.5	6.33	0.1
3	6.33	0.1
3.5	6.34	0.1
4	6.35	0.1
4.5	6.35	0.1
5	6.35	0.1
5.5	6.35	0.1
6	6.36	0.1

6.5	6.35	0.1
7	6.36	0.1
7.5	6.35	0.1
8	6.34	0.1
8.5	6.33	0.03
8.8	6.29	0.03
8.9	6.17	0.03
9	5.82	0.02
9.05	5.57	0.02
9.1	5.21	0.02
9.15	4.72	0.02
9.2	4.14	0.02
9.25	3.52	0.02
9.3	2.94	0.02
9.35	2.3	0.02
9.4	1.78	0.02
9.45	1.27	0.02
9.5	0.88	0.01
9.55	0.54	0.01
9.6	0.36	0.01
9.65	0.21	0.01
9.7	0.12	0.01
9.75	0.073	0.002
9.8	0.05	0.002
9.85	0.037	0.002
9.9	0.033	0.002
9.95	0.03	0.002
10	0.027	0.002
10.05	0.025	0.002
10.1	0.023	0.002
10.15	0.021	0.002
10.2	0.02	0.002
10.25	0.018	0.002
10.3	0.017	0.002
10.35	0.017	0.002
10.4	0.016	0.002
10.5	0.014	0.002
10.6	0.012	0.001
10.7	0.011	0.001
10.8	0.01	0.001
10.9	0.009	0.001
11	0.008	0.001
11.1	0.007	0.001

11.2	0.007	0.001
11.4	0.006	0.001
11.6	0.005	0.001
11.8	0.005	0.001
12	0.004	0.001
12.2	0.004	0.001
12.4	0.004	0.001
12.7	0.004	0.001
13	0.004	0.001

Table A.5.: Beam waist measurement at a distance from the Faraday Isolator of $d = (18.05 \pm 0.34)$ cm.

Position razor blade [mm]	Power [mW]	Uncertainty of Power [mW]
0	6.19	0.1
0.5	6.16	0.1
1	6.2	0.1
1.5	6.2	0.1
2	6.22	0.1
2.5	6.22	0.1
3	6.25	0.1
3.5	6.23	0.1
4	6.37	0.1
4.5	6.38	0.1
5	6.39	0.1
5.5	6.4	0.1
6	6.4	0.1
6.5	6.34	0.1
6.55	6.31	0.03
6.6	6.25	0.03
6.65	6.14	0.03
6.7	5.97	0.03
6.75	5.71	0.03
6.8	5.38	0.03
6.85	4.91	0.03
6.9	4.36	0.03
6.95	3.7	0.03
7	3.08	0.03
7.05	2.44	0.03
7.1	1.91	0.03
7.15	1.4	0.03
7.2	0.97	0.01
7.25	0.68	0.01

7.3	0.44	0.01
7.35	0.28	0.01
7.4	0.17	0.01
7.45	0.1	0.01
7.5	0.08	0.01
7.55	0.06	0.01
7.6	0.05	0.01
7.65	0.04	0.005
7.7	0.04	0.005
7.75	0.04	0.005
7.8	0.03	0.005
7.85	0.03	0.005
7.9	0.03	0.005
8	0.03	0.005
8.1	0.03	0.005
8.2	0.02	0.005
8.3	0.02	0.005
8.4	0.02	0.005
8.5	0.02	0.005
8.6	0.02	0.005
8.8	0.02	0.005

Table A.6.: Beam waist measurement at a distance from the Faraday Isolator of $d = (20.38 \pm 0.22)$ cm.

Position razor blade [mm]	Power [mW]	Uncertainty of Power [mW]
0	5.43	0.1
0.5	5.42	0.1
1	5.41	0.1
1.5	5.4	0.1
2	5.39	0.1
2.5	5.37	0.1
2.6	5.37	0.1
2.7	5.31	0.03
2.75	5.26	0.03
2.8	5.2	0.03
2.85	5.09	0.03
2.9	4.91	0.03
2.95	4.72	0.03
3	4.42	0.03
3.05	4.04	0.03
3.1	3.64	0.03
3.15	3.14	0.03

3.2	2.6	0.03
3.25	2.1	0.03
3.3	1.62	0.03
3.35	1.21	0.03
3.4	0.86	0.01
3.45	0.6	0.01
3.5	0.38	0.01
3.55	0.25	0.01
3.6	0.16	0.01
3.65	0.11	0.01
3.7	0.08	0.01
3.75	0.06	0.01
3.8	0.05	0.01
3.85	0.05	0.01
3.9	0.04	0.01
3.95	0.04	0.005
4	0.04	0.005
4.1	0.03	0.005
4.2	0.03	0.005
4.3	0.02	0.005
4.4	0.02	0.005
4.5	0.02	0.005
4.7	0.01	0.005
5	0.01	0.005
5.5	0.01	0.005
6	0	0.005

Table A.7.: Beam waist measurement at a distance from the Faraday Isolator of $d = (22.1 \pm 0.2)$ cm.

Position razor blade [mm]	Power [mW]	Uncertainty of Power [mW]
0	6.51	0.1
0.5	6.5	0.1
1	6.5	0.1
1.5	6.48	0.1
2	6.48	0.1
2.5	6.48	0.1
3	6.44	0.1
3.1	6.44	0.03
3.2	6.44	0.03
3.3	6.43	0.03
3.4	6.42	0.03
3.5	6.41	0.03

3.55	6.41	0.03
3.6	6.4	0.03
3.65	6.38	0.03
3.7	6.36	0.03
3.75	6.31	0.03
3.8	6.22	0.03
3.85	6.09	0.03
3.9	5.91	0.03
3.95	5.69	0.03
4	5.34	0.03
4.05	4.9	0.03
4.1	4.45	0.03
4.15	3.88	0.03
4.2	3.24	0.03
4.25	2.67	0.03
4.3	2.07	0.03
4.35	1.6	0.03
4.4	1.18	0.01
4.45	0.84	0.01
4.5	0.57	0.01
4.55	0.39	0.01
4.6	0.26	0.01
4.65	0.17	0.01
4.7	0.11	0.01
4.75	0.08	0.01
4.8	0.06	0.01
4.85	0.05	0.01
4.9	0.04	0.005
4.95	0.04	0.005
5	0.04	0.005
5.1	0.03	0.005
5.2	0.03	0.005
5.3	0.03	0.005
5.4	0.02	0.005
5.5	0.02	0.005
5.6	0.02	0.005
5.7	0.02	0.005
5.8	0.02	0.005
5.9	0.02	0.005
6	0.02	0.005

Table A.8.: Beam waist measurement at a distance from the Faraday Isolator of $d = (25.83 \pm 0.1)$ cm.

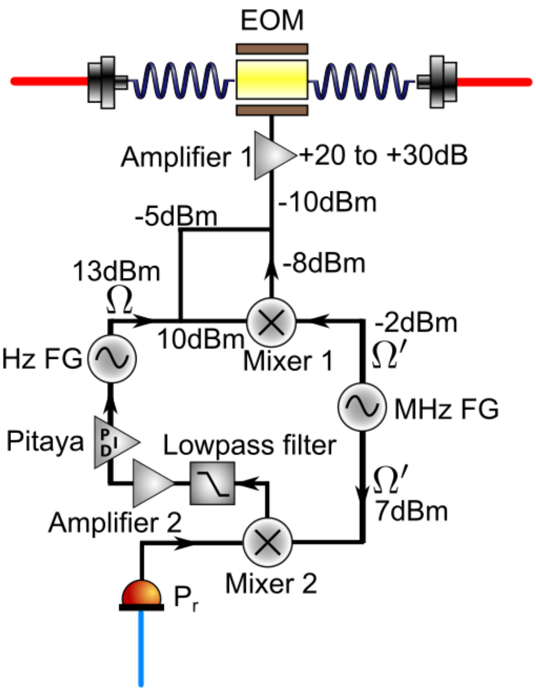

Figure A.2.: More precise description of the circuit. The RIGOL function generator is used as LO for Mixer 1 (ZFM-150+), but since the original signal should be kept and added later on, it is split up with a T-piece leading to -3 dB in each arm. Mixer 1 needs a LO of 10 dBm according to the specs. Therefore, the RIGOL FG needs to be set at 13 dBm. The MHz FG creates the IF for Mixer 1 (modulation signal). According to mixer saturation measurements (see fig. A.3), this can have a maximum power of 5 dBm, however, we need the overall output signal that goes to Amplifier 1 to be as high as possible but before saturation of the amplifier (see fig. A.4). Therefore, the power for IF was chosen to be -2 dBm. The output will be at -8 dBm. The other arm of the split RIGOL FG signal undergoes some attenuation, such that in the end it has a power of -5 dBm. Those two paths are added up such that the power of the center peak will be at -10dBm. This enters Amplifier 1 that adds a certain gain in dB depending on the frequency (see. A.1). The amplified signal is then sent to the EOM. Furthermore, second output of the MHz FG outputs the LO signal for Mixer 2 (demodulation signal), which has to be at 7 dBm. This is mixed with the photodiode signal P_r as RF and outputs an error signal as IF. This passes through a lowpass filter with 1 MHz boundary and is then amplified by Amplifier 2 until it is processed to the PID of the Red Pitaya, that modulates the output frequency of the RIGOL FG.

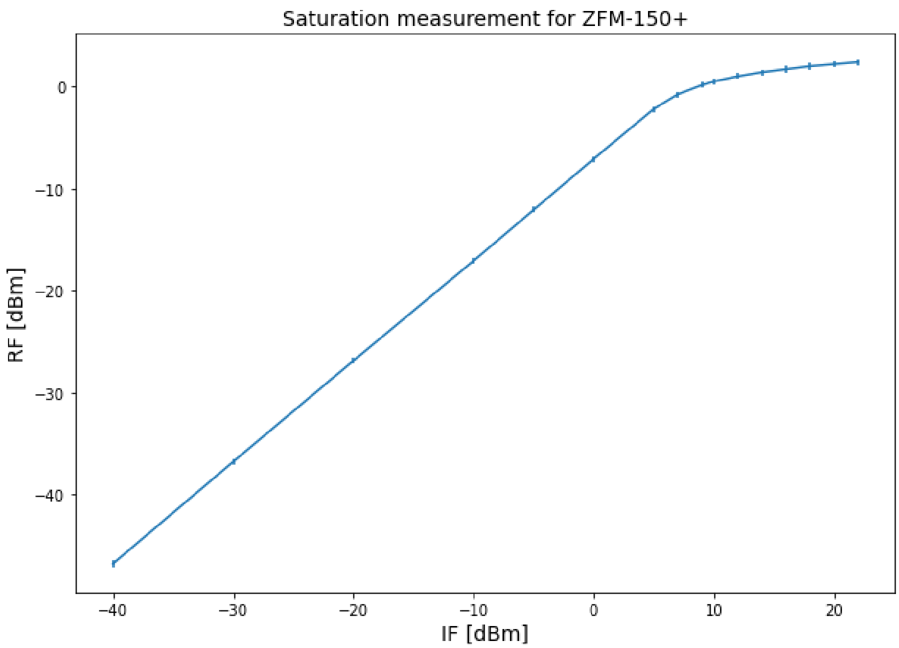

Figure A.3.: Saturation measurement of the frequency mixer "ZMF-150+". It saturates at IF = 5 dBm and RF = -2 dBm.

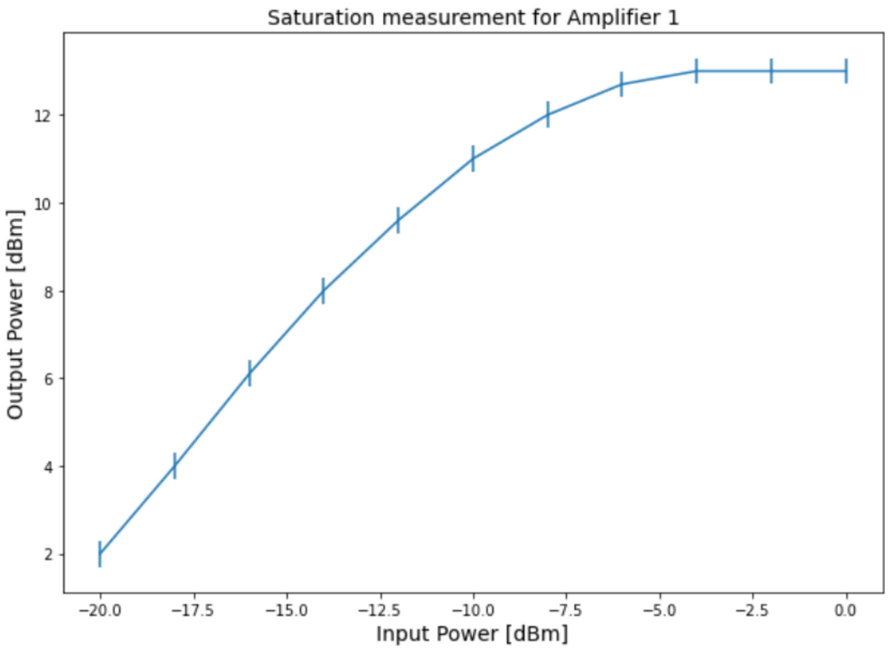

Figure A.4.: Saturation measurement of the amplifier "APT3-04000800-1010-D4", conducted at a frequency of 500 MHz, therefore $g \approx 20$. It starts to saturate at an input power of -10 dBm.

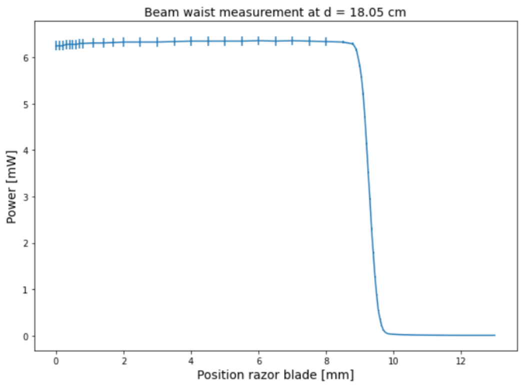

(a) d = (18.05±0.34) cm

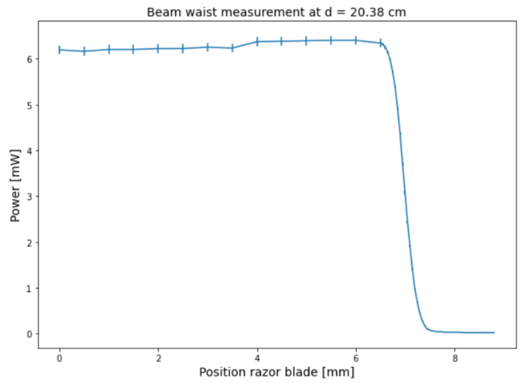

(b) d = (20.38±0.22) cm

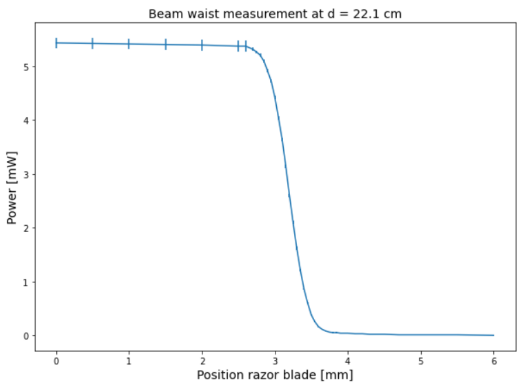

(c) d = (22.1±0.2) cm

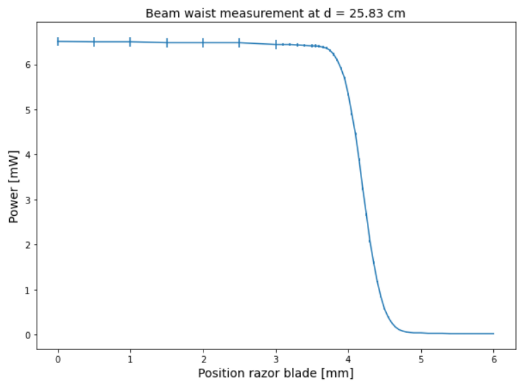

(d) d = (25.83±0.1)

Figure A.5.: Beam waist measurement at different positions d with the output of the Faraday Isolator being the zero position.

B. List of Programs

In this thesis, the used programming scripts are written in Python and Mathematica. In the following, a list of all used scripts including a short description can be found. The mathematica scripts were mostly written by my supervisor Rainer Kaltenbaek and our colleagues from Ljubljana.

B.1. Python scripts

1. **server_get_channel_average_22_08_22_2.py**: This program was used for the first attempt of locking the cavity. It is running on the operating system of the Red Pitaya and streams the PID_{out} values from the PID output. It is called "server" since it is one part of a TCP/IP connection, that requires two programs (a server and a client) that run on different operating systems in order to establish a fast communication between those two. The streamed PID values are sent to the client program 2 via the TCP/IP connection.

2. **client_windows_22_08_22.py**: This is the client program related to 1. It is running on the OS of the lab computer, which is connected to the RIGOL FG. It converts the received data of the server into frequency values and sends them to the FG that adapts its output frequency according to the received value.

3. **client_windows_piezo_06_07_2023.py**: This is again a client program belonging to another TCP/IP connection. It runs on the lab computer and was developed in order to scan through the high-finesse cavity and follow the filering cavity resonance mode at the same time. It changes the output frequency of the RIGOL FG and sends the value by how much the frequency changed to the corresponding server program 4.

4. **server_piezo_06_07_2023.py**: This is the server program related to 3. It runs on a different Red Pitaya, namely the one that drives the piezo. This time, it receives frequency values from the client and converts them into a voltage value that will be applied to the Red Pitaya output that drives the piezo.

5. **Plot&Fit-1Lorentzian.ipynb**: This python script is used to perform the Lorentzian fits that are needed to estimate the linewidth of both the filtering and high-finesse cavity.

6. **Different plots.ipynb**: This python script is used to plot different kinds of data, such as the graphs shown in figures 3.8b, 3.8a, 3.7 etc.

B.2. Mathematica scripts

1. **gausspropagation.nb**: This mathematica script includes all necessary formulas in order to characterize a Gaussian beam.

2. **BeamWaist_positions1&4.nb**: This script (as well as the script below 3) allows to enter measurement data from a razor blade measurement and fits the data such that the beam width can be determined. Then it suggests solutions for the beam waist and its position.

3. **BeamWaist_positions2&3.nb**: See 2.

4. **cavity_find_lens.nb**: This script is used to choose the correct lens to couple into the filtering cavity. It characterizes the cavity properties and matches them to the Gaussian profile of our laser beam.